

Protein Folding as a Jamming Transition

Alex T. Grigas ^{1,2} Zhuoyi Liu ^{3,2} Jack A. Logan ³ Mark D. Shattuck ⁴ and Corey S. O'Hern ^{3,1,2,5,6}

¹Graduate Program in Computational Biology and Biomedical Informatics, [Yale University](#), New Haven, Connecticut 06520, USA

²Integrated Graduate Program in Physical and Engineering Biology, [Yale University](#), New Haven, Connecticut 06520, USA

³Department of Mechanical Engineering, [Yale University](#), New Haven, Connecticut 06520, USA

⁴Benjamin Levich Institute and Physics Department, [The City College of New York](#), New York, New York 10031, USA

⁵Department of Physics, [Yale University](#), New Haven, Connecticut 06520, USA

⁶Department of Applied Physics, [Yale University](#), New Haven, Connecticut 06520, USA



(Received 15 May 2024; revised 30 September 2024; accepted 3 March 2025; published 27 March 2025)

Proteins fold to a specific functional conformation with a densely packed core that controls their stability. Despite their importance, we lack a quantitative explanation for why all protein cores, regardless of their overall fold, possess the same average packing fraction $\langle\phi\rangle \approx 0.55$. However, important developments in the physics of jamming in particulate systems can shed light on the packing of protein cores. Here, we extend the framework of jamming to describe core packing in collapsed polymers, as well as in all-atom models of folded proteins. First, we show in a spherical bead-spring polymer model (with and without bond-angle constraints) that as the hydrophobic interactions increase relative to thermal fluctuations, a jamming-like transition occurs when the core packing fraction exceeds ϕ_c with the same power-law scaling behavior for the potential energy V_r , excess contact number ΔN , and characteristic frequency of the vibrational density of states ω^* versus $\Delta\phi = \phi - \phi_c$ as that for jammed particulate systems. Then, we develop an all-atom model for proteins and find that, above $\phi_c \sim 0.55$, protein cores undergo a jamming-like transition, but with anomalous power-law scaling for V_r , ΔN , and ω^* versus $\Delta\phi$. The all-atom protein model remains close to the native protein structure during jamming and accurately refolds from partially unfolded states.

DOI: [10.1103/PRXLife.3.013018](https://doi.org/10.1103/PRXLife.3.013018)

I. INTRODUCTION

In native solution conditions, globular proteins fold from an extended chain to a compact, functional state. Upon folding, proteins form solvent-inaccessible, or core, regions that include $\sim 10\%$ of the protein [1]. Focusing on hard-core atomic interactions, initial analysis of protein structures found that protein cores are densely packed [2–8]. Numerous prior structural analyses, mutational studies, and theoretical modeling have emphasized that protein energy landscapes are dominated by dense packing in the hydrophobic core [9–17]. More recent atomic structural analyses have shown that the average core packing fraction in proteins (without interatomic overlaps) is $\langle\phi\rangle = 0.55 \pm 0.01$, which raises two key questions [18–22]. First, why do the cores of folded proteins possess a remarkably similar packing fraction? Second, why is the particular value $\langle\phi\rangle \approx 0.55$?

Here, we demonstrate that the dense packing $\langle\phi\rangle \approx 0.55$ in protein cores occurs because they exist near jamming onset. First, we review the key features of the jamming transition in particulate systems, i.e., the power-law scaling of the structural and mechanical properties of jammed sphere packings

with $\Delta\phi = \phi - \phi_c$ where ϕ_c is the onset of jamming. Second, we demonstrate that the final stages of polymer collapse can be described as a jamming transition. When a weakly attractive bead-spring polymer is quenched below the coil-globule and glass transitions [23,24], its interior undergoes a jamming transition at packing fraction $\phi_c \sim 0.63$ with the same power-law scaling behavior for the structural and mechanical properties versus $\Delta\phi$ as found for the jamming transition in particulate systems. We show that ϕ_c can be reduced significantly by adding bond-angle constraints to the bead-spring polymer, yet the power-law scaling behavior with $\Delta\phi$ is the same as that for jammed sphere packings. Finally, we carry out similar studies of hydrophobic collapse for an all-atom protein model with weak attractive nonbonded interactions, as well as constraints on the bond lengths, bond angles, and peptide-bond dihedral angles to maintain proper amino acid stereochemistry. We find that the all-atom protein model collapses as the attractive strength relative to temperature increases and undergoes a jamming-like transition from a floppy to a rigid state near $\phi_c \sim 0.55$ with novel power-law scaling exponents for the structural and mechanical properties versus $\Delta\phi$. These results suggest that proteins collapse until the core amino acids reach a mechanically stable state that resists further compression induced by the hydrophobic interactions. Moreover, the all-atom model can refold proteins from partially unfolded states, suggesting that it captures the protein conformational landscape near the folded state.

Published by the American Physical Society under the terms of the [Creative Commons Attribution 4.0 International](#) license. Further distribution of this work must maintain attribution to the author(s) and the published article's title, journal citation, and DOI.

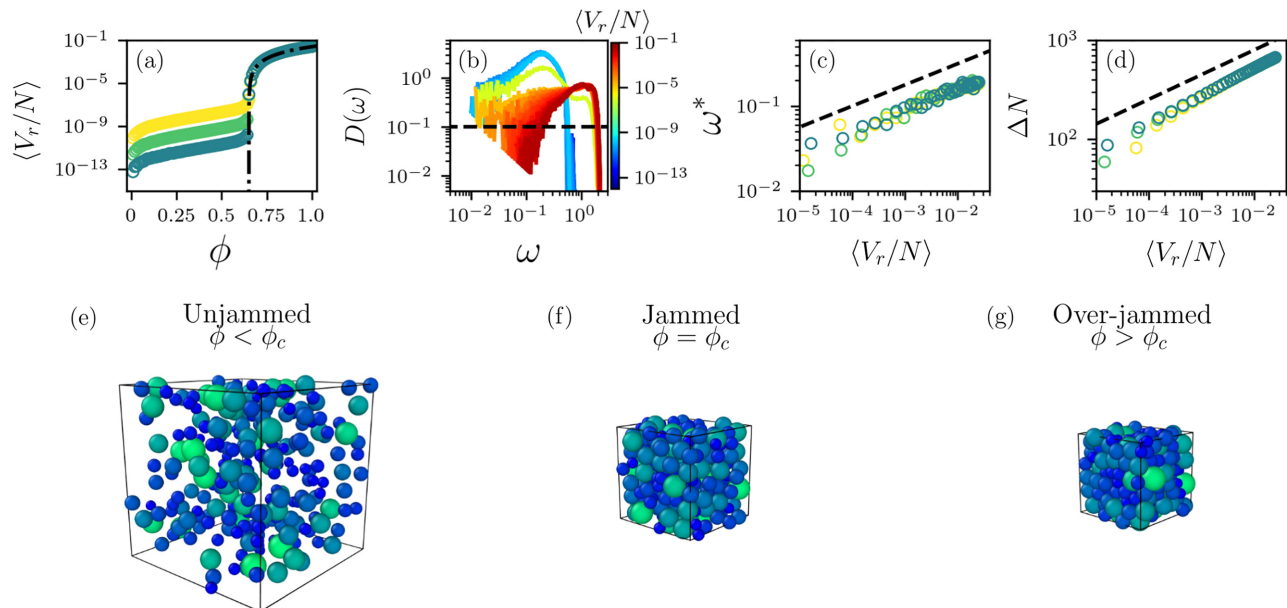


FIG. 1. Hallmarks of the jamming transition during isotropic compression at finite temperatures, $T/\epsilon_r = 10^{-6}$ (yellow), 10^{-7} (green), and 10^{-8} (blue), in collections of repulsive spheres under periodic boundary conditions. (a) The average potential energy per particle $\langle V_r/N \rangle$ plotted vs packing fraction ϕ . The black dot-dashed lines indicate fits to Eq. (3) with $\delta = 2$. (b) The vibrational density of states $D(\omega)$ plotted vs frequency ω at each ϕ colored by $\langle V_r/N \rangle$ increasing from blue to red for $T/\epsilon_r = 10^{-8}$. The black dashed lines indicate the cutoff in $D(\omega) < 10^{-1}$ for determining the characteristic frequency ω^* . (c) ω^* plotted vs $\langle V_r/N \rangle$. (d) The excess number of (nonbonded) contacts above isostaticity ΔN plotted vs $\langle V_r/N \rangle$. The black dashed lines indicate a slope of 1/4. Visualizations of repulsive spheres undergoing compression in periodic boundary conditions (black box) at packing fractions (e) below, (f) near, and (g) above ϕ_c . The color indicates the monomer diameter size increasing from blue (σ_s) to green (σ_{\max}).

II. IDENTIFYING JAMMING TRANSITIONS IN REPULSIVE SYSTEMS AT FINITE TEMPERATURES UNDER CONFINEMENT

We first review the jamming transition of repulsive systems during compression in periodic boundary conditions at finite temperatures for both collections of repulsive spheres and a single repulsive spherical bead-spring polymer. For the repulsive spheres, we assume that they interact via the purely repulsive linear spring potential,

$$\frac{V_{\text{mb}}(r_{ij})}{\epsilon_r} = \frac{1}{2} \left(1 - \frac{r_{ij}}{\sigma_{ij}} \right)^2 \Theta \left(1 - \frac{r_{ij}}{\sigma_{ij}} \right), \quad (1)$$

where r_{ij} is the separation between particles i and j , $\sigma_{ij} = (\sigma_i + \sigma_j)/2$ is the average diameter, and $\Theta(\cdot)$ is the Heaviside step-function. The total potential energy for systems containing repulsive spheres is $V_r = \sum_{i>j} V_{\text{mb}}(r_{ij})$ summed over all overlapping pairs. For illustrative purposes, we present results for $N = 256$ particles, averaged over 20 packings for each value of ϕ during compression. To prevent crystallization, σ_i is randomly selected from a power-law size distribution, $P(\sigma_i) = A\sigma_i^{-3}$, with minimum and maximum diameters σ_s and $\sigma_{\max} = 2.2\sigma_s$ and polydispersity $D = (\langle \sigma_i^2 \rangle - \langle \sigma_i \rangle^2) / \langle \sigma_i \rangle^2 \sim 0.23$ [25].

We also study jamming of a single bead-spring polymer undergoing isotropic compression. Neighboring spherical beads i and $j = i + 1$ on the polymer are bonded via

double-sided linear spring interactions,

$$\frac{V_b(r_{ij})}{\epsilon_b} = \frac{1}{2} \left(1 - \frac{r_{ij}}{\sigma_{ij}} \right)^2, \quad (2)$$

where $\epsilon_b = \epsilon_r$. The nonbonded interactions for the bead-spring polymer are purely repulsive, and thus the total potential energy $V_r = \sum_{i>j} V_{\text{mb}}(r_{ij}) + \sum_{i,j=i+1} V_b(r_{ij})$.

To initialize the systems with purely repulsive spheres, we randomly place the spheres within a periodic box without overlaps at an initial packing fraction $\phi = 0.01$, where $\phi = \sum_{i=1}^N v_{p,i}/v_b$, $v_{p,i}$ is the volume of particle i , and v_b is the volume of the box. To initialize the repulsive bead-spring polymer, we generate an excluded volume random walk within a periodic box. For both systems, we apply affine, isotropic compression in small steps of $\delta\phi = 10^{-3}$, with each compression followed by energy minimization, until the system reaches a target packing fraction ϕ [26]. We then carry out Langevin dynamics [27] at constant temperatures $T/\epsilon_r = 10^{-6}$, 10^{-7} , and 10^{-8} .

To identify jamming onset, we quantify two distinct types of power-law scaling relations for the structural and mechanical properties versus $\Delta\phi$ [28–31]. First, in Fig. 1(a) we show that below a critical packing fraction ϕ_c , $\langle V_r/N \rangle$ increases slowly with ϕ . However, above ϕ_c , the total potential energy increases as a power-law,

$$\langle V_r/N \rangle \sim (\phi - \phi_c)^\delta, \quad (3)$$

where for the purely repulsive linear spring potential, $\delta = 2$, and $\phi_c \approx 0.64$ for the system sizes, particle size

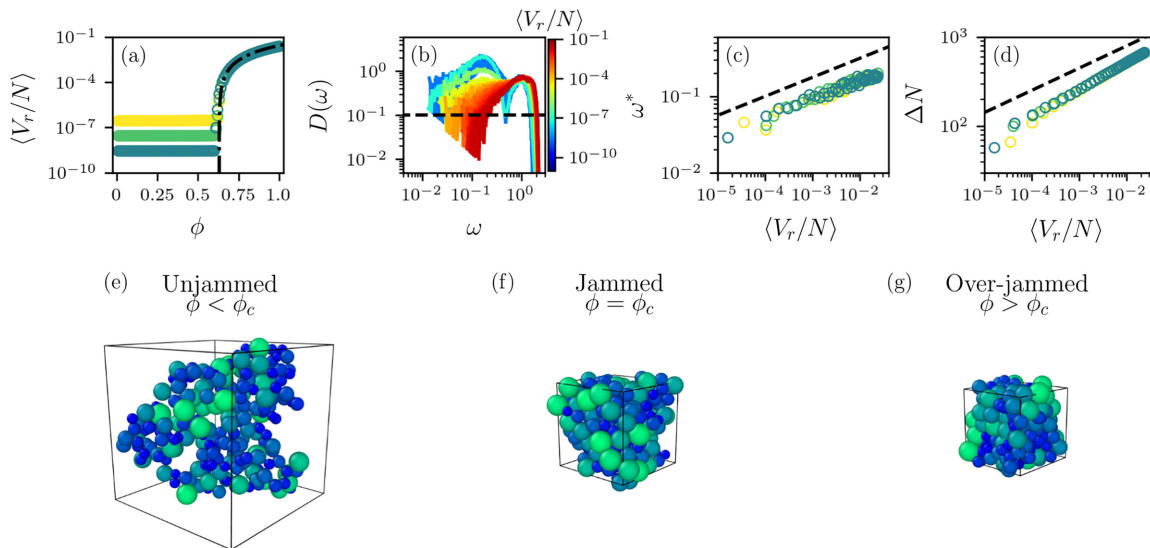


FIG. 2. Hallmarks of the jamming transition during isotropic compression at finite temperatures, $T/\epsilon_r = 10^{-6}$ (yellow), 10^{-7} (green), and 10^{-8} (blue), for a single repulsive bead-spring polymer under periodic boundary conditions. (a) The average potential energy per particle $\langle V_r/N \rangle$ plotted vs packing fraction ϕ . The black dot-dashed lines indicate fits to Eq. (3) with $\delta = 2$. (b) The vibrational density of states $D(\omega)$ plotted vs frequency ω at each ϕ colored by $\langle V_r/N \rangle$ increasing from blue to red for $T/\epsilon_r = 10^{-8}$. The black dashed lines indicate the cutoff in $D(\omega) < 10^{-1}$ for determining the characteristic frequency ω^* . (c) ω^* plotted vs $\langle V_r/N \rangle$. (d) The excess number of (nonbonded) contacts above isostaticity ΔN plotted vs $\langle V_r/N \rangle$. The black dashed lines indicate a slope of $1/4$. Visualizations of a single bead-spring polymer repulsive spheres undergoing compression in periodic boundary conditions (black box) at packing fractions (e) below, (f) near, and (g) above ϕ_c . The color indicates the monomer diameter size increasing from blue (σ_s) to green (σ_{\max}).

polydispersity, and compression protocol used here. As $T \rightarrow 0$, the plateau in $\langle V_r/N \rangle \rightarrow 0$ for $\phi < \phi_c$, and the jamming transition becomes more distinct. We show in Fig. 2(a) that a similar jamming transition occurs during compression of a single repulsive bead-spring polymer. We note two small differences. First, $\langle V_r/N \rangle$ plateaus for $\phi < \phi_c$ instead of increasing slowly and is larger than that for repulsive spheres due to the additional bond constraints. Second, $\phi_c \sim 0.63$ is slightly decreased compared to that for jammed repulsive spheres. While previous studies have obtained jammed packings of bonded spheres that are just as dense as jammed disconnected spheres [32,33], single bead-spring polymers jam at slightly lower ϕ_c in periodic boundary conditions [24,34,35].

A hallmark of the jamming transition can also be found in the system's mechanical properties. Unjammed systems possess many low-frequency, liquid-like modes in the vibrational density of states (VDOS). Near jamming onset in repulsive spheres, excess intermediate frequency modes, known as the boson peak, occur in the VDOS, and as ϕ increases above jamming onset, the boson peak decreases [36–38]. We calculate the VDOS from the eigenvalues e_n of the displacement correlation matrix $S = \mathcal{V}C^{-1}$, where $\mathcal{V}_{ij} = \langle v_i v_j \rangle$ is the velocity correlation matrix, $C_{ij} = \langle (r_i - r_i^0)(r_j - r_j^0) \rangle$ is the positional covariance matrix, v_i are the sphere velocities, and r_i and r_i^0 are the instantaneous and average sphere positions. The angle brackets indicate time averages. The VDOS $D(\omega_n)$ is then obtained by binning the frequencies $\omega_n = \sqrt{e_n}$, where the frequencies are given in units of $\sqrt{\epsilon_r/(m\sigma_s^2)}$ and m is the mass of each sphere [39,40].

In Figs. 1(b) and 2(b), we plot the VDOS for repulsive spheres and the bead-spring polymer as a function of

$\langle V_r/N \rangle$ (increasing from blue to red) for $T/\epsilon_r = 10^{-8}$. We find that when the total potential energy is small, the VDOS possesses many liquid-like modes. As $\langle V_r/N \rangle$ increases, a low-frequency, non-Debye plateau forms near jamming onset, and the plateau decreases as the system is further compressed. The main difference in the VDOS for repulsive spheres and the bead-spring polymer is that the VDOS for the bead-spring polymer has a peak at $\omega = 1$ for all ϕ , which corresponds to the bond-length fluctuations. The formation of the plateau in the VDOS can be quantified by the characteristic frequency ω^* at which $D(\omega^*)$ falls below a small threshold. Previous studies of jamming in repulsive spheres have found that ω^* obeys the power-law scaling relation $\omega^* \sim \langle V \rangle^\zeta$, where $\zeta = 1/4$, and $\langle V \rangle$ is the average potential energy [24,41]. We show in Figs. 1(c) and 2(c) that $\omega^* \sim (\langle V_r/N \rangle)^\zeta$ above jamming onset for repulsive spheres and the collapsed bead-spring polymer, respectively, where $\zeta = 1/4$.

The number of interparticle contacts controls the transition from floppy to rigid states, i.e., at jamming onset, collections of repulsive spheres become isostatic with the same number of contacts as degrees of freedom $N_c = N_{\text{iso}} = dN - N_0 + 1$, where d is the spatial dimension and N_0 is the number of zero modes from d rigid translations and underconstrained spheres. We can determine N_0 from the number of zero eigenvalues of S . In Fig. 1(d), we show that above ϕ_c , the average excess number of contacts above isostaticity $\Delta N = \langle N_c \rangle - N_{\text{iso}}$ scales with the same exponent $\zeta = 1/4$ versus potential energy as that found for the scaling exponent for ω^* versus $\langle V_r/N \rangle$. In addition, we find the same power-law scaling exponent for ΔN versus $\langle V_r/N \rangle$ for the bead-spring polymer, where $\Delta N = \langle N_c \rangle + N_b - N_{\text{iso}}$, where $N_b = N - 1$ is the number of polymer bonds, and N_0 is the number of zero modes

[see Fig. 2(d)]. We show collections of repulsive spheres and a single repulsive bead-spring polymer undergoing isotropic compression in a periodic box for packing fractions below, at, and above jamming onset in Figs. 1(e)–1(g) and Figs. 2(e)–2(g).

Taken together, the power-law scaling relations for $\langle V_r/N \rangle$, ω^* , and ΔN above ϕ_c indicate jamming transitions that occur in collections of repulsive particles and a single repulsive bead-spring polymer during isotropic compression in periodic boundary conditions. Computational studies of jamming have largely been restricted to repulsive systems under confinement. Below, we extend studies of jamming to attractive bead-spring polymers under open boundary conditions to understand whether the same power-law scaling relations for the structural and mechanical properties hold during polymer collapse.

III. ONSET OF JAMMING DURING COLLAPSE OF ATTRACTIVE BEAD-SPRING POLYMERS

Here, we show that a uniformly attractive spherical bead-spring polymer undergoes a jamming transition during collapse. In this case, the compaction is not applied through the boundary conditions as for studies of jamming transitions in collections of repulsive particles, rather it is induced through the attractive, hydrophobic interactions between monomers in the polymer under open boundaries. As shown in Sec. II, repulsive (nonbonded and bonded) spheres undergo a jamming transition with power-law scaling of the structural and mechanical properties versus $\Delta\phi$ when they are compressed above jamming onset at sufficiently low temperatures. To model nonbonded attractive interactions within bead-spring polymers, we modify the repulsive spring potential in Eq. (1) by extending the interaction distance to $r_{\beta}/\sigma_{ij} = 1 + \sigma_{ij}\beta_{ij}/\sigma_s$, and we cut off the interactions at $r_{\alpha}/\sigma_{ij} = 1 + \alpha > r_{\beta}$ using a piecewise harmonic function of r_{ij} :

$$\frac{V_a(r_{ij})}{\epsilon_r} = \begin{cases} \frac{1}{2}\left(1 - \frac{r_{ij}}{\sigma_{ij}}\right)^2 - V_c/\epsilon_r & \text{for } r_{ij} \leq r_{\beta}, \\ -\frac{k}{2\epsilon_r}\left(\frac{r_{ij}}{r_{\alpha}} - 1\right)^2 \Theta\left(1 - \frac{r_{ij}}{r_{\alpha}}\right) & \text{for } r_{ij} > r_{\beta}, \end{cases} \quad (4)$$

where $V_c/\epsilon_r = (k/\epsilon_r)(r_{\beta}/r_{\alpha} - 1)^2/2 + (1 - r_{\beta}/\sigma_{ij})^2/2$ to ensure continuity. α defines the attractive range, and $\beta_{ij} = \beta\lambda_{ij}$ defines the magnitude of the attractive force between beads i and j . For uniformly attractive bead-spring polymers, $\lambda_{ij} = 1$ for all pairs. Additionally, we use the same size distribution $P(\sigma_i)$ as in Sec. II. Neighboring beads i and $j = i + 1$ on the polymer are bonded via double-sided linear spring interactions as in repulsive bead-spring polymers [Eq. (2)]. Because there is no confining box for the attractive bead-spring polymer, we must define a new approach for calculating the local ϕ . To calculate the average core packing fraction $\langle\phi\rangle$, we identify core beads as those with zero exposed surface area measured using the Richards-Lee spherical probe algorithm with probe size $\sigma_p/\sigma_s = 0.73$, as is commonly used to calculate the solvent accessible surface area for proteins [42,43]. The packing fraction of core bead i is $\phi_i = v_i^b/v_i^v$, where v_i^b and v_i^v are the volumes of bead i and its enclosing Voronoi cell [44]. The average core packing fraction is $\langle\phi\rangle = n_c^{-1} \sum_{i=1}^{n_c} \phi_i$, where n_c is the number of core

beads in the polymer. Our choice of σ_p/σ_s is similar to the size ratio of alanine to a water molecule, but our results are insensitive to this choice.

To study the collapse of bead-spring polymers, we carry out Langevin dynamics [27] under open boundary conditions for attractive range $0.5 \leq \alpha \leq 2$, attractive depth $10^{-12} \leq \beta \leq 10^{-3}$, and temperature $10^{-8} \leq T/\epsilon_r \leq 10^{-6}$. The simulations are initialized from a collapsed structure generated by an excluded-volume random walk where the system is energy-minimized after each bead is placed [26]. In Fig. 3(a), we plot $\langle\phi\rangle$ versus the attractive strength $\alpha^2\beta$, which demonstrates that the attractive strength controls the available free volume in the core analogous to the pressure (or total potential energy) in purely repulsive systems. [See Figs. 3(d)–3(f) for visualizations of typical conformations.] When the attractive strength is low, thermal expansion dominates and the core unpacks. As $\alpha^2\beta$ increases, a plateau in $\langle\phi\rangle$ forms, followed by an overcompressed regime. $\langle\phi\rangle$ versus $\alpha^2\beta$ is well fit by

$$\langle\phi\rangle = A(\alpha^2\beta)^a - B(\alpha^2\beta)^{-b} + \phi_c, \quad (5)$$

where A and B are constants, $\phi_c \rightarrow 0.63$, and the exponents $a \rightarrow 1$ and $b \rightarrow 1$ as $T/\epsilon_r \rightarrow 0$. Note the similarity between ϕ_c in the collapsed attractive bead-spring polymer and jammed repulsive packings shown in Sec. II.

To identify jamming onset, we calculate $V_r/\epsilon_r = \sum_{i>j} V_{mb}(r_{ij})/\epsilon_r + \sum_{(i,j=i+1)} V_b(r_{ij})/\epsilon_r$, where the first sum is over distinct nonbonded pairs and the second sum is over bonded pairs. In Fig. 3(b), we plot the time-averaged $\langle V_r/N \rangle$ versus $\alpha^2\beta$. We find that $\langle V_r/N \rangle \sim V_0$, where $V_0 \sim T/\epsilon_r$ for $\alpha^2\beta < T/\epsilon_r$. However, when $\alpha^2\beta > T/\epsilon_r$, $\langle V_r/N \rangle$ increases from the plateau value V_0 as a power-law:

$$\langle V_r/N \rangle - V_0 = C(\alpha^2\beta)^c, \quad (6)$$

where C is a constant and $c \rightarrow 2$ as $T/\epsilon_r \rightarrow 0$. Thus, when $\langle\phi\rangle > \phi_c$, $\langle V_r/N \rangle$ increases strongly, which indicates a jamming transition. In Fig. 3(c), we combine data from Figs. 3(a) and 3(b). For $\langle\phi\rangle < \phi_c$, $\langle V_r/N \rangle \sim V_0$. When $\langle\phi\rangle > \phi_c$, $\langle V_r/N \rangle$ increases as a power-law, which can be obtained by combining Eqs. (5) and (6):

$$\langle\phi\rangle = \mathcal{A}(\Delta V_r)^{a/c} + \mathcal{B}(\Delta V_r)^{-b/c} + \phi_c, \quad (7)$$

where $\Delta V_r = \langle V_r/N \rangle - V_0$, $\mathcal{A} = A/C^{a/c}$, and $\mathcal{B} = B/C^{-b/c}$. When $\langle\Delta\phi\rangle \gg 0$, Eq. (7) simplifies to $\langle\Delta V_r/N\rangle \sim \langle\Delta\phi\rangle^{\delta}$ [Eq. (3)], where $\delta = c/a \rightarrow 2$ in the $T/\epsilon_r \rightarrow 0$ limit, which is the same scaling exponent found for jamming of repulsive spheres and the repulsive bead-spring polymer in Sec. II [28]. The potential energy for collapsed bead-spring polymers increases as a power-law above a characteristic ϕ in the same way that the potential energy scales with ϕ above jamming onset for disconnected and connected repulsive spheres. For two-dimensional (2D) attractive bead-spring polymers, we find similar behavior for $\langle V_r/N \rangle$ versus $\alpha^{d-1}\beta$ in d spatial dimensions.

We quantify the rigidity of attractive bead-spring polymers by calculating the eigenvalues of the displacement correlation matrix as in Sec. II. In Fig. 4(a), we plot the VDOS for attractive bead-spring polymers as a function of $\langle V_r/N \rangle$.

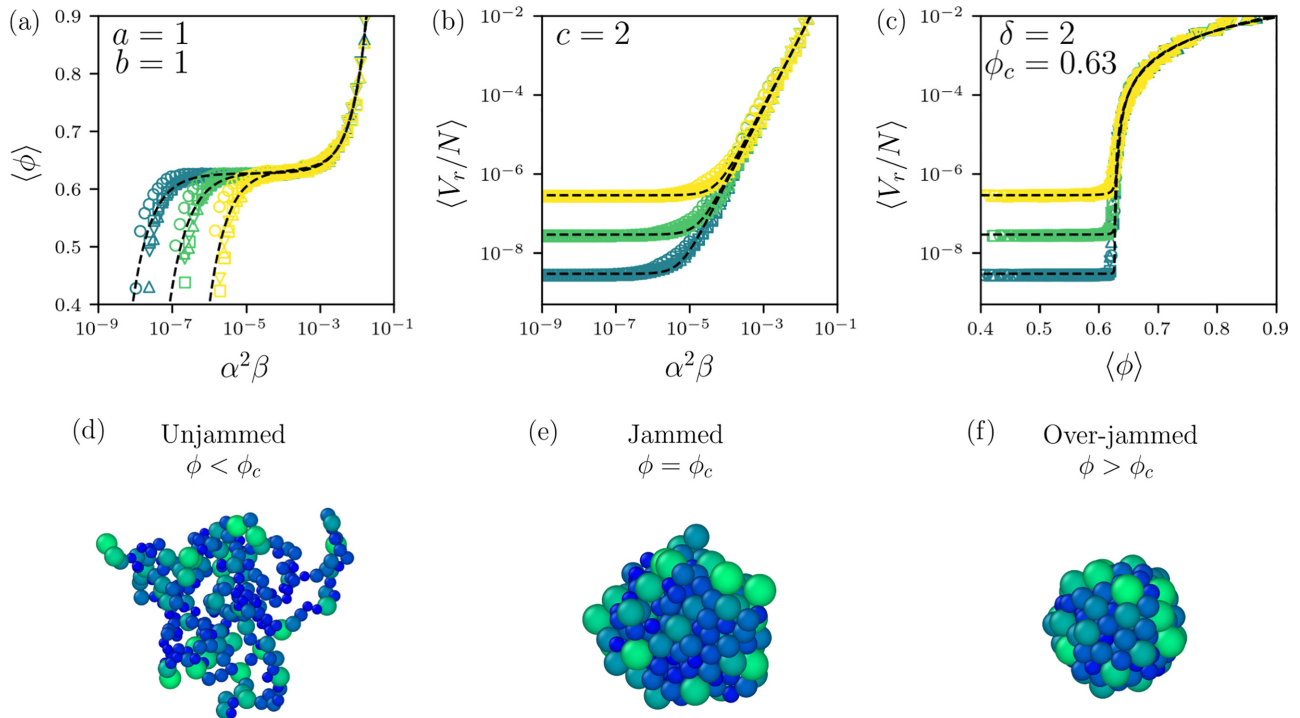


FIG. 3. (a) Average core packing fraction $\langle \phi \rangle$ plotted vs strength of the attractive interactions $\alpha^2 \beta$ for bead-spring polymers at temperatures $T/\epsilon_r = 10^{-6}$ (yellow), 10^{-7} (green), and 10^{-8} (blue) and $\alpha = 0.5$ (circles), 1.0 (squares), 1.5 (upward triangles), and 2.0 (downward triangles). The black dashed lines indicate fits to Eq. (5) with $a = b = 1$. (b) Average pair potential energy $\langle V_r/N \rangle$ plotted vs $\alpha^2 \beta$. The black dashed lines indicate fits to Eq. (6) with $c = 2$. (c) $\langle V_r/N \rangle$ plotted vs average core packing fraction $\langle \phi \rangle$. The black dashed lines indicate fits to Eq. (7). At large $\langle \phi \rangle$, $\langle V_r/N \rangle - V_0 \sim (\langle \phi \rangle - \phi_c)^\delta$, where $\delta = c/a = 2$ and $\phi_c = 0.63$. (d)–(f) Visualizations of attractive bead-spring polymers at packing fractions below, near, and above ϕ_c . The color indicates the monomer diameter increasing from blue (σ_s) to green (σ_{\max}).

We find that when the potential energy is low, the system displays many liquid-like modes. As $\langle V_r/N \rangle$ increases, a low-frequency, non-Debye plateau forms near jamming onset, and the plateau decreases as the system further collapses. The plateau in the VDOS can be quantified by the characteristic frequency ω^* at which $D(\omega^*)$ falls below a small threshold. We show in Fig. 4(b) that $\omega^* \sim (\langle V_r/N \rangle / \alpha)^\zeta$ above jamming onset for collapsed bead-spring polymers, where $\zeta = 1/4$ is the same as that found for jamming of collections of repulsive spheres and the repulsive bead-spring polymer. Note that di-

viding $\langle V_r/N \rangle$ by α collapses the data for different attractive ranges as previously reported [24].

An essential feature of the jamming transition is isostaticity, i.e., systems rigidify when the number of (nonredundant) constraints equals the number of degrees of freedom. While the number of nonredundant constraints is difficult to determine in 3D packings with finite-ranged interactions that can be either attractive or repulsive, we have shown previously that packings interacting via Eq. (4) are isostatic when contacts are defined for separations between nonbonded pairs

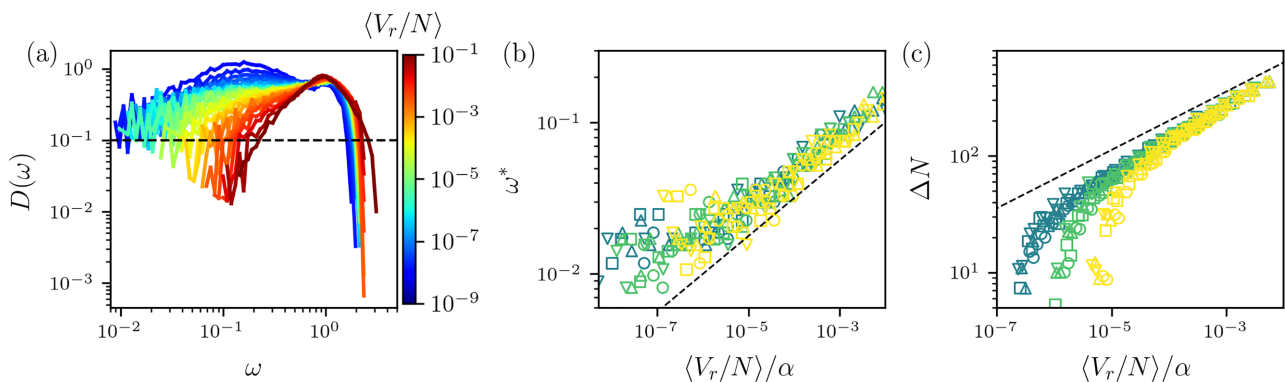


FIG. 4. (a) Vibrational density of states $D(\omega)$ for attractive bead-spring polymers for average potential energy $\langle V_r/N \rangle$ (in units of ϵ_r) increasing from 10^{-9} (blue) to 10^{-1} (red). The black dashed line indicates $D(\omega^*) = 10^{-1}$. (b) The characteristic plateau frequency ω^* and (c) average excess number of contacts above the isostatic value $\langle \Delta N \rangle$ plotted vs $\langle V_r/N \rangle / \alpha$. The black dashed lines in (b) and (c) have slope $1/4$.

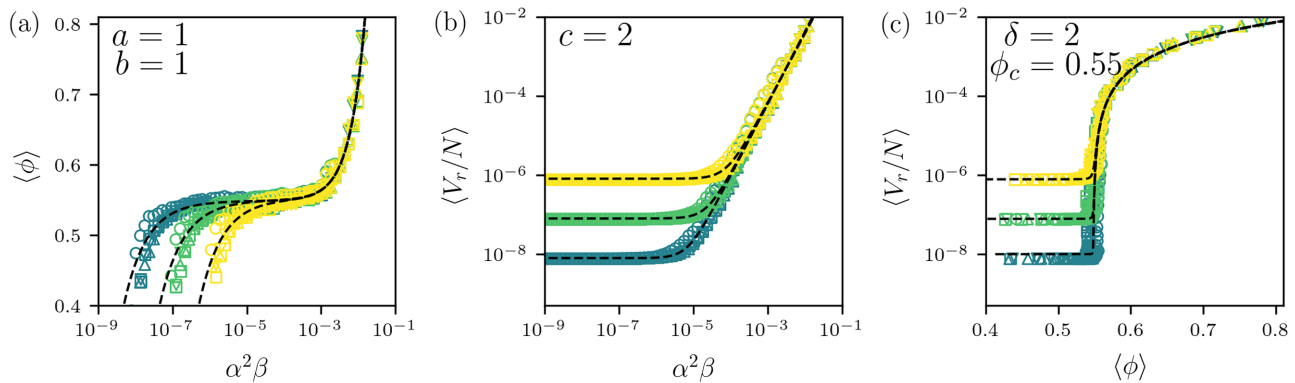


FIG. 5. (a) Average core packing fraction $\langle\phi\rangle$ plotted vs strength of the attractive interactions $\alpha^2\beta$ for bead-spring polymers with random bond-angle constraints at temperatures $T/\epsilon_r = 10^{-6}$ (yellow), 10^{-7} (green), and 10^{-8} (blue) and $\alpha = 0.5$ (circles), 1.0 (squares), 1.5 (upward triangles), and 2.0 (downward triangles). The black dashed lines indicate fits to Eq. (5) with $a = b = 1$. (b) Average pair potential energy $\langle V_r/N \rangle$ plotted vs $\alpha^2\beta$. The black dashed lines indicate fits to Eq. (6) with $c = 2$. (c) $\langle V_r/N \rangle$ plotted vs average core packing fraction $\langle\phi\rangle$. The black dashed lines indicate fits to Eq. (7). At large $\langle\phi\rangle$, $\langle V_r/N \rangle - V_0 \sim \langle\phi - \phi_c\rangle^\delta$, where $\delta = c/a = 2$ and $\phi_c = 0.55$.

with $r_{ij} < r_\beta$ [24,45,46]. In Fig. 4(c), we plot $\Delta N = N_c(r_{ij} < r_\beta) + N_b - N_{\text{iso}}$ versus $\langle V_r/N \rangle/\alpha$, where N_b is the number of polymer bonds, $N_{\text{iso}} = dN - N_0$, and N_0 is the number of zero modes. The excess contact number follows the same power-law scaling relation $\Delta N \sim \langle V_r \rangle^\zeta$ with $\zeta = 1/4$ as that found for jamming of repulsive spheres and polymers. Thus, the collapse of weakly attractive bead-spring polymers belongs to the same universality class as that for jamming of disconnected and connected, repulsive spheres.

IV. COLLAPSE OF ATTRACTIVE BEAD-SPRING POLYMERS WITH BOND-ANGLE CONSTRAINTS

In the previous section, we showed that the ϕ_c values for jammed repulsive polymer packings and the cores of collapsed attractive bead-spring polymers with only bond-length constraints are similar to that for jammed sphere packings. However, the inclusion of bond-angle constraints changes the persistence length of bead-spring polymers, which can lower the core packing fraction [34,47]. Here, we incorporate bond-angle constraints into the potential energy function that describes attractive bead-spring polymers in Sec. III. For every bond angle θ_{ijk} between consecutive beads i , $j = i + 1$, and $k = i + 2$, we add the bond-angle harmonic restraint,

$$\frac{V_a(\theta_{ijk})}{\epsilon_a} = \frac{1}{2}(\theta_{ijk} - \theta_{ijk}^0)^2, \quad (8)$$

where $\epsilon_a = \epsilon_b$ is the energy scale of bond-angle fluctuations, and θ_{ijk}^0 is the equilibrium bond angle selected from a uniform random distribution. To identify jamming onset, we measure $V_r/\epsilon_r = \sum_{i>j} V_{\text{mb}}(r_{ij})/\epsilon_r + \sum_{(i,j=i+1)} V_b(r_{ij})/\epsilon_r + \sum_{(i,j=i+1,k=j+1)} V_a(r_{ij})/\epsilon_r$, where the first sum is over distinct nonbonded pairs, the second sum is over bonded pairs, and the third sum is over bond-angle triplets. In Fig. 5, we show that the bond-angle restraint has a significant effect on the core packing fraction, resulting in $\phi_c = 0.55$. However, note that the power-law scaling of $\langle\Delta V_r/N\rangle$ with $\Delta\phi$ is the same with and without bond-angle constraints even though the ϕ_c values are different.

V. A STEREOCHEMICALLY ACCURATE REPULSIVE ALL-ATOM PROTEIN MODEL

In this section, we develop a stereochemically accurate all-atom model for proteins to investigate jamming in the context of core formation in proteins. The guiding principle in the development of the all-atom protein model is to restrain the minimum components of protein stereochemistry necessary to sample experimentally accurate protein conformations. For the bonded interactions, we add restraints on the bond lengths r_{ij} , bond angles θ_{ijk} , and dihedral angles involving double bonds ω_{ijkl} to the respective equilibrium values r_{ij}^0 , θ_{ijk}^0 , and ω_{ijkl}^0 that occur in each target protein's x-ray crystal structure:

$$\frac{V_b(r_{ij})}{\epsilon_b} = \frac{1}{2\sigma_H^2}(r_{ij} - r_{ij}^0)^2, \quad (9)$$

$$\frac{V_a(\theta_{ijk})}{\epsilon_a} = \frac{1}{2}(\theta_{ijk} - \theta_{ijk}^0)^2, \quad (10)$$

$$\frac{V_d(\omega_{ijkl})}{\epsilon_d} = \frac{1}{2}(\omega_{ijkl} - \omega_{ijkl}^0)^2, \quad (11)$$

where $\epsilon_b = \epsilon_a = \epsilon_d = \epsilon_r$ are the respective energy scales, and σ_H is the diameter of hydrogen. We set the energy parameters to be equal to weight nonbonded overlaps and deformations in protein stereochemistry equally. We add restraints to the main chain peptide bond dihedral angles, known as ω , which, due to the peptide bond's partial double-bonded character, are relatively planar in high-quality protein structures. For amino acids with side chains containing double bonds, we also add dihedral angle restraints to maintain their planar geometry for phenylalanine, tyrosine, histidine, and tryptophan.

Nonbonded interactions are modeled as repulsive steric interactions with weak hydrophobic attractions [Eq. (4)]. As proteins are molecular systems, the selection of a set of repulsive atom sizes $\{\sigma_i\}$ is not straightforward, and many sets have been used [2–8,18,48]. We must also consider the backbone dihedral angles of rotatable single bonds within amino acids. The backbone dihedral angles φ and ψ are known to take on certain values in high-resolution structures, and amino acids with φ and ψ outside of these known bounds are termed

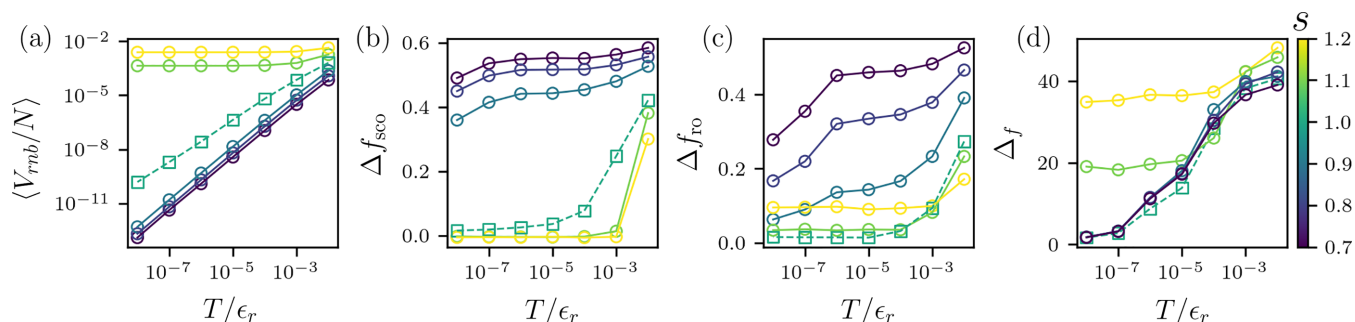


FIG. 6. (a) The average repulsive overlap energy ($\langle V_{\text{rmb}}/N \rangle$) is plotted vs the temperature T/ϵ_r . The difference in the fraction of outliers in the (b) backbone dihedral angles and (c) side chain dihedral angles between the all-atom protein models (without attractions) and x-ray crystal structures of proteins plotted vs T/ϵ_r . (d) Root-mean-square deviation in the C_α atom positions Δ_f (in Å) between the all-atom protein model and the experimental structures plotted vs T/ϵ_r . The atom sizes $\{\sigma_i\}$ are scaled by $s = 0.7$ – 1.2 colored from purple to yellow with circular markers. The data for $s = 1$ from the main text are highlighted using dashed lines and square markers.

Ramachandran outliers [49–52]. Similarly, each amino acid side chain takes on particular dihedral angles, called rotamers, that most frequently occur. Whether experimentally obtained protein structures or computational models sample the correct backbone and side chain dihedral angle distributions is typically determined by the community software MOLPROBITY [50–52].

To ensure that computational models possess the correct backbone and side chain dihedral angle distributions, most all-atom force fields include explicit restraints [53–57]. However, Ramachandran *et al.* first demonstrated that by assuming only repulsive, hard-core atomic interactions, one can recapitulate the backbone dihedral angles φ and ψ that occur in proteins as those that do not cause large interatomic overlaps [58,59]. Recent studies have also shown that a similar approach can recapitulate the side chain dihedral angle distributions in x-ray crystal structures of proteins given an appropriate set of atom sizes [60–64]. We therefore employ a set of atom sizes $\{\sigma_i\}$ that give rise to large interatomic overlaps when the backbone and side chain dihedral angles populate *unallowed* dihedral angle combinations. (See Table III in Appendix A.)

To validate the atom sizes in the all-atom protein model, we carry out Langevin dynamics simulations with no attractions [i.e., $\alpha = \beta = 0$ in Eq. (4)] starting from the energy-minimized protein x-ray crystal structures over a wide range of temperatures. We study 50 single-chain proteins with no disulfide bonds randomly selected from a dataset of high-resolution x-ray crystal structures [65,66]. The protein sizes range from $N_{\text{aa}} = 60$ to 524 amino acids with an average of $\langle N_{\text{aa}} \rangle = 180$. (PDBIDs are given in Table IV in Appendix A.) We use the MOLPROBITY software to assess the degree to which the backbone and side chain dihedral angles sample allowed conformations during the simulations. Even high-quality x-ray crystal structures possess some fraction of Ramachandran f_{ro} and side chain f_{sco} dihedral angle outliers. Therefore, we report the difference between the experimental and simulation fraction of outliers Δf_{ro} and Δf_{sco} . We conduct simulations with the atom sizes $\{\sigma_i\}$ in Table III, as well as scaling them by s to quantify the sensitivity of the MOLPROBITY metrics on the atom sizes.

As shown in Fig. 6(a), for $s \leq 1$, as the temperature is lowered, the all-atom protein models sample more hard-sphere-like conformations with fewer nonbonded overlaps quantified

as the repulsive overlap energy $V_{\text{rmb}} = \sum_{i>j} V_{\text{rmb}}(r_{ij})$ summed over all overlapping nonbonded pairs [Eq. (1)]. However, for $s > 1$, the atom sizes are so large that atomic overlaps occur even at low temperatures, and $\langle V_r/N \rangle$ is nearly constant with decreasing T . In Figs. 6(b) and 6(c), we show that when $s = 1$ and $T/\epsilon_r \lesssim 10^{-5}$, both the Ramachandran backbone and side chain dihedral angle outliers relative to the outliers in the high-resolution x-ray crystal structure database approach zero. When the atom sizes are decreased with $s < 1$, even in the low-temperature limit, the all-atom protein model samples a large number of backbone and side chain dihedral angle outliers. The side chain dihedral angles are particularly sensitive, increasing from $\Delta f_{\text{sco}} \sim 0$ for $s = 1$ to $\Delta f_{\text{sco}} > 0.35$ for $s = 0.9$. In addition, increases in the atom sizes (with $s > 1$) lead to a larger plateau in Δf_{ro} , yet few side chain dihedral angle outliers, likely because the large overlaps shown in Fig. 6(a) lock the initial x-ray crystal structure dihedral angles into place.

We also calculate the root-mean-square deviations (RMSDs) in the C_α positions between the simulated and experimental structures,

$$\Delta = \sqrt{\frac{1}{N_{\text{aa}}} \sum_{m=1}^{N_{\text{aa}}} (\vec{r}_{ms} - \vec{r}_{me})^2}, \quad (12)$$

where \vec{r}_{ms} and \vec{r}_{me} are the C_α positions of the m th amino acid from the simulations and x-ray crystal structures, respectively. In Fig. 6(d), we show that the root-mean-squared deviations of the final simulation backbone C_α atoms from the experimental structure Δ_f increase significantly due to large nonbonded atomic overlaps.

For $s > 1$, the atoms cannot be considered as nearly hard spheres because there are large overlaps between nonbonded atoms resulting in the repulsive all-atom protein model rapidly unfolding under constant temperature dynamics. Most all-atom force fields for proteins use van der Waals radii that are larger than the atom sizes we employ. (See Table III in Appendix A for a comparison of the atom sizes used in the present study to those used in the Amber force field [48].) For all atoms except hydrogen, $s > 1$ when comparing the atom sizes from our all-atom protein model to those used in the Amber force field. Since other all-atom models for proteins

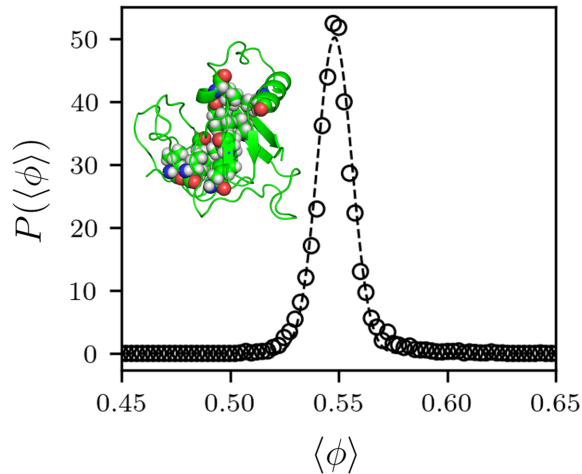


FIG. 7. The probability distribution $P(\langle\phi\rangle)$ of the average core packing fraction $\langle\phi\rangle$ from high-resolution protein x-ray crystal structures (black circles) fit to a Gaussian with average and standard deviation $\langle\phi\rangle = 0.55 \pm 0.01$. Inset: PDBID: 5juh from the x-ray crystal structure database. The main chain is shown as a ribbon diagram, and the interior, core residues are rendered as spheres.

use $s > 1$, large attractive forces and explicit restraints on the backbone and side chain dihedral angles are needed to recapitulate the distributions found in x-ray crystal structures of proteins [53–57]. In this way, our all-atom protein model has the minimal elements necessary to capture high-resolution x-ray crystal structures.

VI. A SELF-CONSISTENT CALCULATION OF PROTEIN CORE PACKING

While the packing fraction of protein cores has been quantified numerous times since the first x-ray crystal structures were solved, the literature provides a wide range of atomic sizes $\{\sigma_i\}$ [2–8,18,48]. With the atom sizes defined and validated in Sec. V, we calculate the core packing fraction using a dataset of ~ 5000 high-quality x-ray crystal structures with a resolution $< 1.8 \text{ \AA}$ culled from the Protein Data Bank (PDB) using the PISCES software with all hydrogens placed using the REDUCE software [65–67]. The relative solvent-accessible surface area (rSASA) is measured using the Lee-Richards algorithm with a spherical probe the size of a water molecule, and core residues are defined as those with $\text{rSASA} \leq 10^{-3}$ [42,43]. The packing fraction of core residue i is $\phi_i = v_i^b/v_i^v$, where v_i^b is the nonoverlapping volume of the core amino acid, and v_i^v is the volume of its enclosing Voronoi cell [44]. The average core packing fraction is $\langle\phi\rangle = n_c^{-1} \sum_{i=1}^{n_c} \phi_i$, where n_c is the number of core residues. We have previously found that protein cores in experiments possess an average packing fraction of $\langle\phi\rangle = 0.55 \pm 0.01$, as shown in Fig. 7 [18,19,21,22].

VII. PROTEIN CORE FORMATION DESCRIBED AS A JAMMING TRANSITION

Does the jamming transition that describes bead-spring polymer collapse apply to protein core formation? As

described in Sec. V, to construct an all-atom protein model analogous to the bead-spring polymer model, we enforce the correct stereochemistry of the amino acids using harmonic potentials on the bond lengths, bond angles, and peptide bond dihedral angles. Nonbonded interactions are modeled using Eq. (4), where $\lambda_{ij} = (\lambda_i + \lambda_j)/2$ is the average hydrophobicity associated with atom pairs i and j , and $0 \leq \lambda_i \leq 1$ is the hydrophobicity per amino acid that is assigned to each atom on a given amino acid [68]. (See Table V in Appendix A.) To explore the dynamics of protein core formation in the all-atom model, we carry out Langevin dynamics starting from the energy-minimized x-ray crystal structure (using $\alpha = \beta = 0$ to remove initial atomic overlaps) for all 50 studied proteins. (See Table IV in Appendix A.) In Fig. 8(a), we plot the packing fraction of core residues $\langle\phi\rangle$ averaged over the 50 proteins versus increasing attractive strength. At small $\alpha^2\beta$, the proteins unfold and $\langle\phi\rangle < 0.55$. As the attractive interactions increase, a plateau at $\langle\phi\rangle \sim 0.55$ (i.e., at the average packing fraction of experimentally determined protein cores) occurs for $\alpha^2\beta \sim T/\epsilon_r$. Increasing the attraction further causes a steep increase in $\langle\phi\rangle$. As T/ϵ_r is lowered, the all-atom model behaves similarly to the bead-spring polymer, and the plateau extends to smaller $\alpha^2\beta$. $\langle\phi\rangle$ versus $\alpha^2\beta$ is well fit by the power-law scaling in Eq. (5), where $\phi_c \rightarrow 0.55$ and the exponents $a \rightarrow 1/3$ and $b \rightarrow 2$ as $T/\epsilon_r \rightarrow 0$, notably different from the exponents for the attractive bead-spring polymer.

Furthermore, when we plot the sum of the average total nonbonded repulsive potential energy and bonded potential energy per atom $\langle V_r/N \rangle$ versus $\alpha^2\beta$ in Fig. 8(b), we find that $\langle V_r/N \rangle \sim V_0$, where $V_0 \sim T/\epsilon_r$ for $\alpha^2\beta < T/\epsilon_r$. However, when $\alpha^2\beta > T/\epsilon_r$, $\langle V_r/N \rangle$ increases from the plateau value V_0 as a power-law in $\alpha^2\beta$ [Eq. (6)], where $c \rightarrow 3/2$ as $T/\epsilon_r \rightarrow 0$. Thus, we find that when $\langle\phi\rangle > \phi_c$, the total pair potential energy per atom increases strongly, which indicates a jamming-like transition. In Fig. 8(c), we combine data from Figs. 8(a) and 8(b). For $\langle\phi\rangle < \phi_c$, $\langle V_r/N \rangle \sim V_0$. When $\langle\phi\rangle > \phi_c$, $\langle V_r/N \rangle$ increases as a power law in $\langle\phi\rangle - \phi_c$ as in Eq. (7). In Fig. 8(c), we show that $\delta' = 9/2$, which is larger than the exponent $\delta = 2$ obtained for collapsed bead-spring polymers.

We also determine the VDOS for the all-atom protein model by calculating the eigenvalues of S for the backbone C_α atoms as a function of $\langle\phi\rangle$. In Fig. 9(a), we show the VDOS for the all-atom protein model; it displays similar features as a function of $\langle V_r/N \rangle$ to those found near jamming onset for the weakly attractive bead-spring polymer. However, the power-law scaling of the characteristic frequency $\omega^* \sim \langle V_r/N \rangle^{\zeta'}$ [Fig. 9(b)] has a larger exponent $\zeta' = 1/3$ than that found for collapsed bead-spring polymers.

To calculate the number of excess contacts above isostaticity ΔN for the all-atom protein model, we must first determine the number of redundant restraints N_r for $\langle\phi\rangle < \phi_c$. Redundant restraints give rise to states of self-stress and do not rigidify the system [69]. In the case of bead-spring polymers, each bond is independent and therefore nonredundant. To calculate the number of zero modes N_0 for the unjammed system with $\langle\phi\rangle < \phi_c$, we minimize the all-atom model ($\alpha = 0$) for each protein, numerically calculate the dynamical matrix $M = \partial^2 V_r / (\partial r_i \partial r_j)$ with respect to the backbone C_α atom positions, and count the number of zero eigenmodes of M . According to Maxwell-Calladine constraint counting,

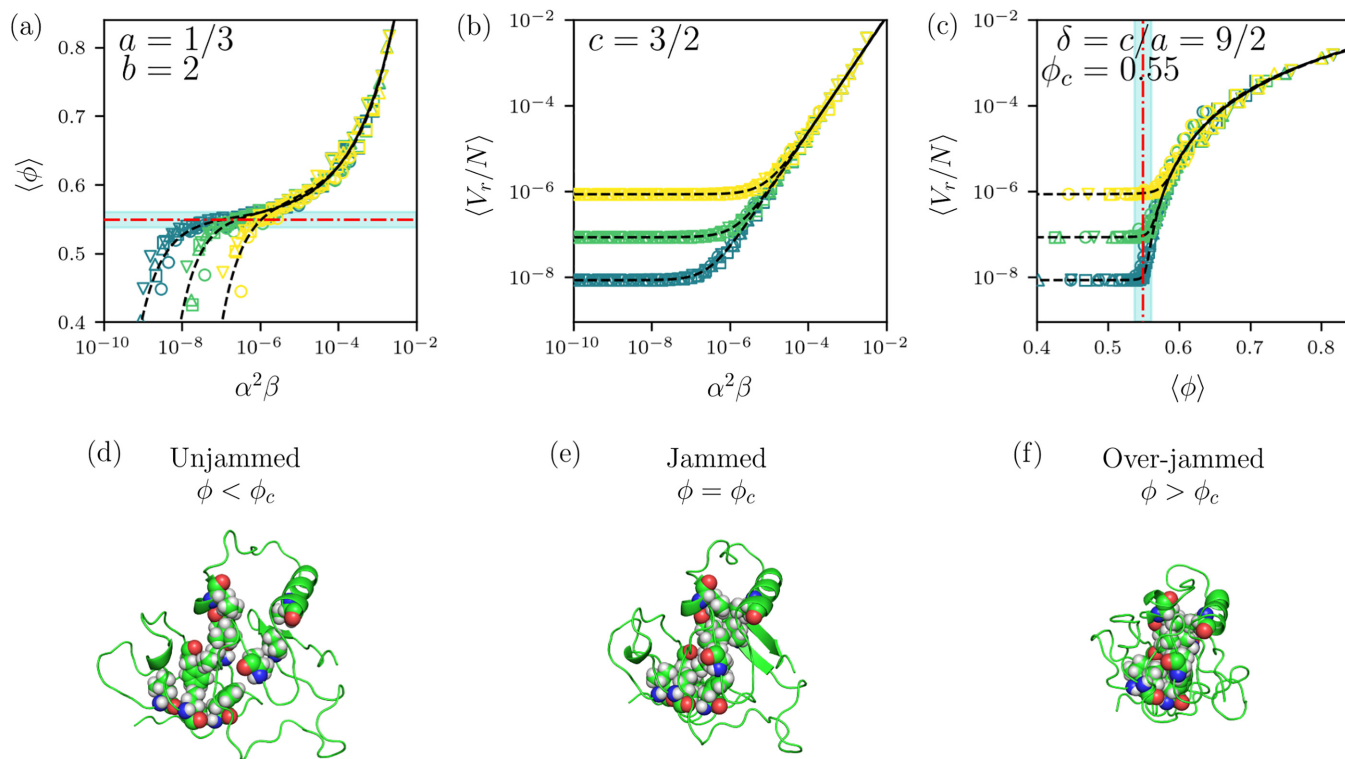


FIG. 8. (a) The average core packing fraction $\langle\phi\rangle$ plotted vs the attraction strength $\alpha^2\beta$ for the all-atom protein model for temperatures $T/\epsilon_r = 10^{-6}$ (yellow), 10^{-7} (green), and 10^{-8} (blue) and $\alpha = 0.5$ (circles), 1.0 (squares), 1.5 (upward triangles), and 2.0 (downward triangles). The red dot-dashed line and cyan shading indicate the average and standard deviation of the core packing fraction in the x-ray crystal structure dataset. The black dashed lines indicate fits to Eq. (5) with $a = 1/3$ and $b = 2$. (b) The average potential energy per atom $\langle V_r/N\rangle$ plotted vs $\alpha^2\beta$. The black dashed lines indicate fits to Eq. (6) with $c = 3/2$. (c) $\langle V_r/N\rangle$ plotted vs $\langle\phi\rangle$. The red dot-dashed line and cyan shading indicate the average and standard deviation of the core packing fraction in the x-ray crystal structure dataset. The black dashed lines indicate fits to Eq. 7. At large $\langle\phi\rangle$, $\langle V_r/N\rangle - V_0 \sim \langle\phi - \phi_c\rangle^{\delta'}$, where $\delta' = c/a = 9/2$ and $\phi_c = 0.55$. (d)–(f) Visualizations of PDBID: 5juh at packing fractions below, near, and above ϕ_c . The backbone is rendered as a ribbon diagram, while the core residues at ϕ_c are shown as spheres.

$dN - N_r = N_0$. Therefore, we can determine N_r and calculate $\Delta N = dN - [N_r + N_c(r_{ij} < r_\beta)]$. In Fig. 9(c), we show that $\Delta N \sim (\langle V_r/N\rangle/\alpha)^{\zeta'}$ with $\zeta' = 1/3$, again larger than $\zeta = 1/4$ found for collapsed bead-spring polymers.

Thus, taken together, Figs. 8 and 9 show that the all-atom protein model undergoes a jamminglike transition when

the average core packing fraction increases above the value observed in x-ray crystal structures. However, the transition to the jammed state in the all-atom protein model displays scaling exponents δ' and ζ' that are larger than those found previously for the jamming transition in repulsive spheres and collapsed bead-spring polymers [24]. These results suggest

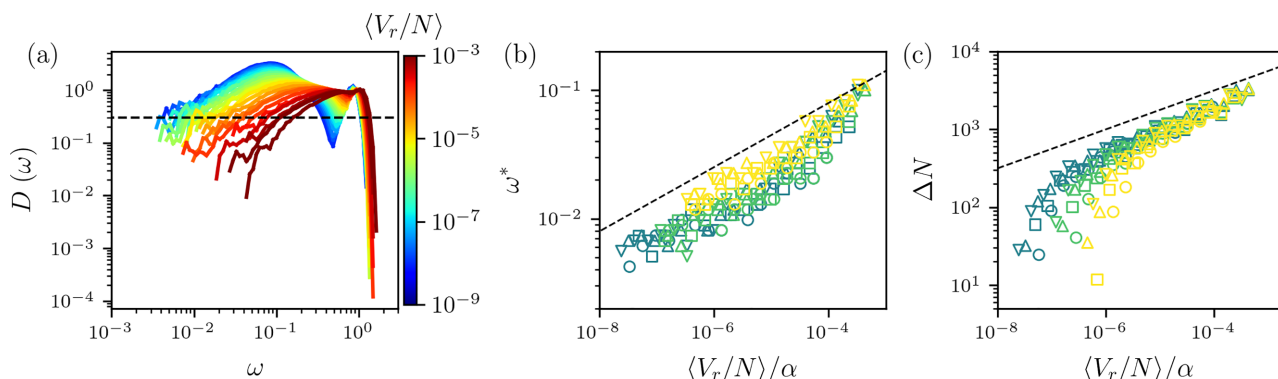


FIG. 9. (a) VDOS for the all-atom protein model as a function of $\langle V_r/N\rangle$ (in units of ϵ_r) increasing from 10^{-9} (blue) to 10^{-1} (red). The black dashed line indicates $D(\omega^*) = 2 \times 10^{-1}$. (b) The characteristic plateau frequency ω^* and (c) average excess number of contacts above the isostatic value $\langle\Delta N\rangle$ plotted vs $\langle V_r/N\rangle/\alpha$. The black dashed lines in (b) and (c) have slope 1/3.

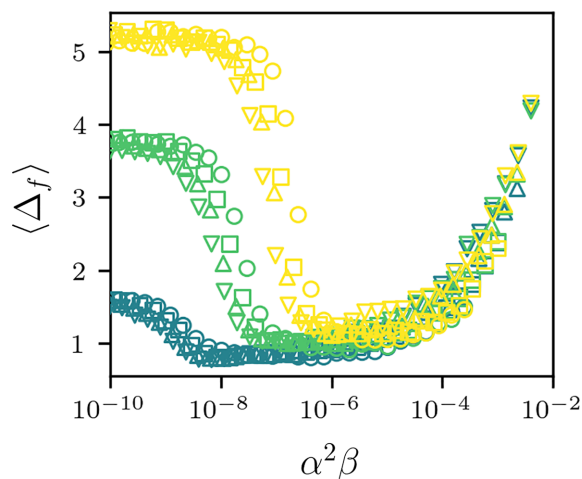


FIG. 10. C_α RMSD $\langle \Delta_f \rangle$ in Å between the all-atom protein models and the x-ray crystal structures averaged over 50 proteins plotted vs $\alpha^2 \beta$ when starting from the experimental structure for temperature $T/\epsilon_r = 10^{-6}$ (yellow), 10^{-7} (green), and 10^{-8} (blue) and $\alpha = 0.5$ (circles), 1.0 (squares), 1.5 (upward triangles), and 2.0 (downward triangles).

that the anomalous scaling exponents are caused by the unique geometry of amino acids and not from nonbonded attractive interactions [70,71].

We have demonstrated that during folding, the all-atom protein model undergoes a jamminglike transition for $\langle \phi \rangle > \phi_c$. We now quantify whether the backbone atoms deviate from the x-ray crystal structures during the collapse process. We calculate the root-mean-square deviations (RMSDs) in the C_α positions between the simulated and experimental structures Δ [Eq. (12)]. We find that Δ converges rapidly versus time, and thus we focus on Δ_f at the last time point. We plot $\langle \Delta_f \rangle$ averaged over the 50 proteins in Fig. 10. We find that $\langle \Delta_f \rangle \sim 1$ Å near jamming onset, confirming that not only the core packing fraction, but also the *global* backbone conformation is nearly identical to the x-ray crystal structure at jamming onset.

VIII. PROTEIN REFOLDING

Does the C_α RMSD of the all-atom model relative to the x-ray crystal structures remain small when the simulations are initialized further from the x-ray crystal structure? To study the ability of the all-atom model to refold proteins, we initialize the simulations with conformations at different C_α RMSD Δ_i using conformations generated by the model with no attractions ($\alpha = \beta = 0$), which unfold over time. We then carry out Langevin dynamics simulations of the all-atom model with attractions at $T/\epsilon_r = 10^{-7}$ over the range $0.5 \leq \alpha \leq 5.5$, and we set β such that $\alpha^2 \beta \sim T/\epsilon_r$. In Fig. 11, we plot the long-time C_α RMSD $\langle \Delta_f \rangle$ versus Δ_i for a range of α averaged over all 50 proteins. We find that for short attractive ranges (i.e., $\alpha \lesssim 0.5$), while starting in the crystal structure can lead to a jamming transition, the model cannot refold (i.e., $\langle \Delta_f \rangle \sim \Delta_i$) above $\Delta_i \sim 2$ Å. As α is increased, the model can refold initial states with $\Delta_i \lesssim 5$ Å to $\langle \Delta_f \rangle \sim 2$ Å, a threshold that is considered properly folded in all-atom MD simulations

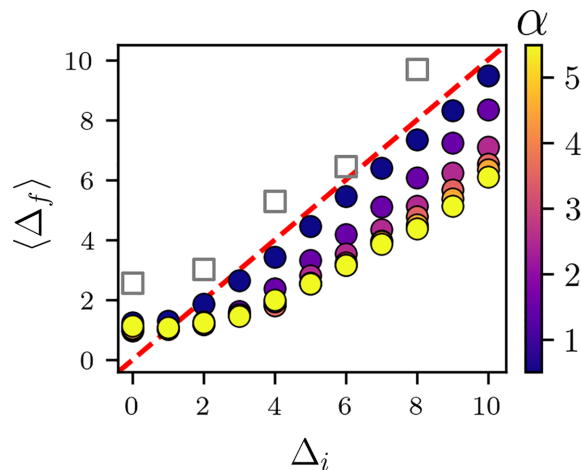


FIG. 11. The final average C_α RMSD $\langle \Delta_f \rangle$ (in Å) plotted vs the initial C_α RMSD Δ_i in Å for $T/\epsilon_r = 10^{-7}$. The filled circles are colored by $\alpha = 0.5$ –5.5 increasing from purple to yellow, and β is set so that $\alpha^2 \beta \sim T/\epsilon_r$. All-atom MD simulations of a single protein (PDBID: 2igp) using the Amber99SB-ILDN force field are shown as gray squares. The red dashed line indicates $\langle \Delta_f \rangle = \Delta_i$.

of protein folding [72]. In addition, all proteins that refold form a well-defined core with $\langle \phi \rangle \sim 0.55$.

To compare refolding of our all-atom attractive protein model to results from current all-atom force fields for proteins, we carried out MD simulations of the $N = 114$ residue globular protein PDBID: 2igp using the Amber99SB-ILDN force field [54,73] starting from several partially unfolded states with C_α RMSD Δ_i from the x-ray crystal structure. The MD simulations were carried out in a periodic dodecahedron-shaped box that is sufficiently large such that the protein surface is at least 20 Å from the box edges. The simulation box was solvated with water molecules modeled using TIP3P at neutral pH and 0.15M NaCl [74,75]. Short-range van der Waals and screened Coulomb interactions were truncated at 1.2 nm, while long-ranged electrostatic interactions were tabulated using the particle mesh Ewald summation method. The LINCS algorithm was used to constrain the bond lengths. We performed two energy minimization runs to first relax the protein and then to relax the water molecules and the protein together using the steepest decent algorithm until the maximum net force magnitude on an atom is smaller than $50 \text{ kJ mol}^{-1} \text{ nm}^{-1}$. We perform NVT simulations of the system at temperature $T = 300$ K using a velocity rescaling thermostat for sampling the canonical ensemble [76]. The equations of motion for the atomic coordinates and velocities are integrated using a leapfrog algorithm with a 2 fs time step. We ran 10 simulations for 1000 ns starting from the same protein conformation, but with different initial velocities for each atom randomly selected from a Maxwell-Boltzmann distribution at $T = 300$ K. We then calculated the average C_α RMSD between the simulation structures and the x-ray crystal structure as a function of time.

In Fig. 12(a), we show that when the initial atomic positions are close to the x-ray crystal structure, the C_α RMSD $\langle \Delta \rangle \sim 2$ Å. This result indicates that the closest free-energy minimum of the Amber99SB-ILDN force field is ~ 2 Å from

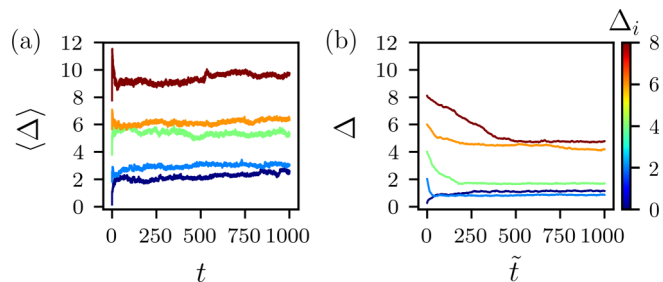


FIG. 12. The average C_α RMSD $\langle \Delta \rangle$ in Å plotted vs time (in ns) from MD simulations of the globular protein PDBID: 2igp using the (a) Amber Amber99SB-ILDN force field. (b) Similar data as in (a) except for the C_α RMSD Δ in Å for a single initial condition from MD simulations of the all-atom protein model in reduced time units $\tilde{t} \sim t/\sqrt{m_H \sigma_H^2/\epsilon_r}$. The line color indicates the initial C_α RMSD Δ_i for $\Delta_i = 0, 2, 4, 6,$ and 8 Å from blue to red.

the experimental structure and that the free-energy barriers are sufficiently large at $T = 300$ K that the system is not able to move away from the minimum. However, for an initial C_α RMSD $\Delta_i > 2$ Å, little refolding is observed and $\langle \Delta \rangle \sim \Delta_i$. The average experimental refolding time at room temperature for a protein of this size is typically larger than $1 \mu\text{s}$ [77]. However, the experimental structures likely refold from completely unfolded states, whereas the simulations shown here start from much smaller initial C_α RMSD of $\Delta_i < 8$ Å. In Fig. 12(b), we show that in contrast to the results for the Amber99SB-ILDN force field, our model (with $\alpha = 2.5$ and $\alpha^2\beta \sim T/\epsilon_r$) is able to refold or partially refold over a wide range of Δ_i . For $\Delta_i \lesssim 4$ Å, $\Delta \lesssim 2$ Å. For $\Delta_i \gtrsim 4$ Å, the protein partially refolds with $\Delta < \Delta_i$ at long times. The Amber99SB-ILDN data are compared to the average refolding result in Fig. 11 as gray squares.

IX. DISCUSSION

We have shown that the collapse of weakly attractive bead-spring polymers displays a jamming-like transition in the same universality class as that for jamming of disconnected, repulsive spheres and that adding polymeric (connectivity and bond-angle) constraints decreases jamming onset at ϕ_c . We further showed that hydrophobic collapse of a stereochemically accurate all-atom protein model displays a jamming-like transition with similar power-law scaling for the structural and mechanical properties of protein cores above $\phi_c \approx 0.55$, but the power-law scaling exponents differ from those for jamming of repulsive spheres. Thus, our results suggest that $\langle \phi \rangle \approx 0.55$ observed in x-ray crystal structures of proteins reflects the onset of a jamming-like transition during hydrophobic collapse.

In this work, we addressed the question of why the cores of most proteins possess similar packing fraction. However, why is it $\langle \phi \rangle \approx 0.55$? To provide insight into this question, we present a brief review of results for the packing fraction at jamming onset ϕ_c for packings of monomers in Table I and for polymer packings in Table II. In general, elongated particles can pack more densely than spheres; however, packings of frictional particles have reduced ϕ_c . In addition, polymeric constraints decrease the jammed packing fraction, relative to

TABLE I. Values of ϕ_c for jammed packings of repulsive monomers with different shapes under periodic boundary conditions (PBC) in three dimensions in the large-system limit. The top eight rows provide data in the rapid cooling and compression rate limit. In the ninth row, ϕ_c increases with decreasing cooling rate. The tenth row shows results using the SWAP Monte Carlo technique for repulsive monodisperse spherical particles.

Monomers	ϕ_c	Boundary
spheres	0.64 [28]	PBC
polydisperse spheres	0.64–0.85 [78]	PBC
ellipses	0.64–0.7 [71,79]	PBC
superellipsoids	0.64–0.75 [80]	PBC
tetra-, octa-, dodeca-, icosahedra	0.76, 0.7, 0.72, 0.7 [81]	PBC
frictional repulsive spheres	0.54–0.64 [82,83]	PBC
bumpy effective frictional spheres	0.54–0.64 [84]	PBC
deformable spheres	0.5–0.76 [85]	PBC
amino acid-shapes	0.55–0.62 [18,21]	PBC
spheres SWAP Monte Carlo	0.64–0.7 [25]	PBC

that for packings of disconnected monomers. Thus, ϕ_c for the all-atom protein model is determined by the competing effects of increased ϕ_c from the elongated shapes of amino acids, decreased ϕ_c from the effective friction of bumpy amino acids, and decreased ϕ_c from bond-length and bond-angle constraints. Future computational studies of intermediate models ranging in detail from simple polymer models to the all-atom protein model will fully demonstrate the competing effects of monomer shape and polymer constraints on the jammed core packing fraction.

We also note in Table I that the ϕ_c values can be tuned by applying different packing-generation protocols [16,24,25,87–90]. The packing-generation protocols presented here were carried out in the rapid cooling and compression rate limits. An important open question is whether slower cooling and compression rates can give rise to larger values of ϕ_c in the all-atom protein model. To further motivate this question, we characterize the core packing fraction for x-ray crystal structures of hen egg white lysozyme that have been obtained at high pressures [91]. In Fig. 13, we plot the average core packing fraction $\langle \phi \rangle$ of these structures versus pressure. We find that $\langle \phi \rangle$ increases dramatically from

TABLE II. Values of ϕ_c for jammed packings of repulsive and attractive polymeric systems under periodic boundary conditions (PBC), spherical boundary conditions (SBC), and open boundary conditions (OBC) in three dimensions in the large-system limit and for rapid cooling and compression protocols.

Polymers	ϕ_c	Boundary
repulsive short bead-spring chains	0.62 [32,34]	PBC
repulsive short angle bead-spring chains	0.1–0.49 [34,47]	PBC
repulsive bead-spring polymer	0.58 [35]	SBC
repulsive bent sphere trimers	0.57–0.62 [86]	PBC
attractive bead-spring polymer	0.63 [This work]	OBC
attractive angle bead-spring polymer	0.55 [This work]	OBC
All-atom protein model	0.55 [This work]	OBC

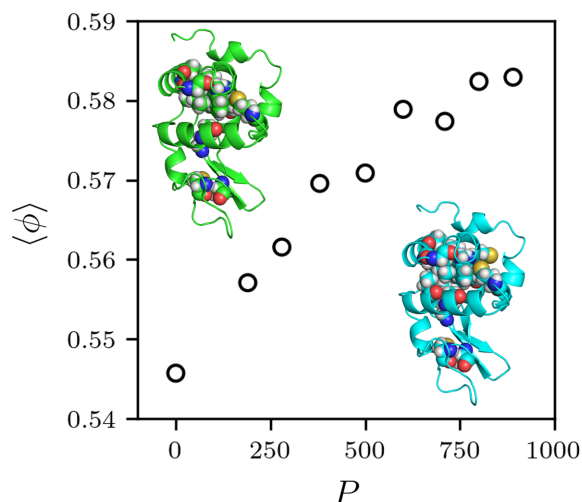


FIG. 13. The average core packing fraction $\langle \phi \rangle$ of hen egg white lysozyme (HEWL) plotted vs pressure (P in MPa). The x-ray crystal structures solved at $P = 0.1$ (PDBID: 4wld) and 890 MPa (PDBID: 4wm5) are visualized in green (top left) and cyan (bottom right), respectively. The backbone is shown as a ribbon diagram, and the solvent-inaccessible core residues are shown as spheres.

$\langle \phi \rangle = 0.55$ to 0.585 at the highest pressures studied. Remarkably, the MOLPROBITY metrics of quality of these high pressure structures are comparable to those for high-resolution x-ray crystal structures at ambient pressure. These results suggest that the cores of these high-pressure structures can potentially occur in our all-atom protein model provided that we employ slow cooling rates. Without a mechanical model, it is difficult to determine whether the high-pressure structures are under large strains with $\Delta\phi > 0$ or whether the pressure has perturbed the structures to a new, denser jammed packing, i.e., that $\phi_c(P = 890 \text{ MPa}) > \phi_c(P = 0.1 \text{ MPa})$. By applying the all-atom protein model developed here, we can determine whether the high-pressure structures are under strain or not, which has important implications for protein binding [92]. Similarly, previous computational studies have suggested that proteins exist in a glassy potential energy landscape, and experimental studies on small proteins have provided evidence that the final stage of protein folding, known as the dry molten-globule, represents slow evolution toward the final fold [93–101].

While identifying ϕ_c is an interesting question, a key insight of the physics of jamming is that the controlling variable is not the jammed packing fraction, but the deviation in packing fraction, $\Delta\phi = \phi - \phi_c$. For example, we showed here that the potential energy, deviation in contact number, and characteristic frequency of the VDOS are controlled by $\Delta\phi$ [28]. Further, other studies of jammed sphere packings have shown that the pressure, specific heat, bulk, and shear moduli also scale with $\Delta\phi$ [30,31]. Note that the power-law scaling exponents can depend on the particular ϕ_c if the configurations at jamming onset possess differing amounts of positional order [102].

Connecting protein core formation and the jamming transition offers several additional directions for future research. For example, the response to point mutations in proteins can

be reformulated as an unjamming or jamming process, which can lead to improved predictions of conformational changes upon mutation [103–105]. Packing at protein-protein interfaces can also be interpreted in the context of jamming, which can provide insight into the scoring of computational models of protein-protein interfaces [106]. In addition, the all-atom model developed here can be used to investigate crowding and sticking interactions that affect *in vivo* protein structure [107]. The results described here can also improve our understanding of the mechanical properties of proteins. Experimental studies have shown that proteins possess a low-frequency boson peak [108,109], which is associated with functional and allosteric large-scale motion of proteins [110,111]. In future studies, we will compare the low-frequency vibrational modes from all-atom models of x-ray crystal structures to known collective motions of proteins.

ACKNOWLEDGMENTS

The authors acknowledge support from NIH Training Grant No. T32GM145452 (A.T.G., C.S.O., and Z.L.), NIH Training Grant No. T15LM007056-37 (J.A.L.), and the High Performance Computing facilities operated by Yale’s Center for Research Computing.

DATA AVAILABILITY

The stereochemically accurate all-atom protein model developed here is available in Ref. [112]. The REDUCE software is needed to add hydrogens to the x-ray crystal structures. All simulations were conducted on a single CPU, and computation time was limited to less than 24 h per simulation.

APPENDIX: STEREOCHEMICALLY ACCURATE ALL-ATOM PROTEIN MODEL PARAMETERS

Here we present the key parameters of the all-atom protein model described in Sec. V. First, in Table III we show the atomic radii σ_i that define the repulsive hard-core interactions. These atom sizes were initially developed by finding the optimal set of atomic radii that, under a purely repulsive interaction, predict the side chain dihedral angle rotamers,

TABLE III. The atomic radii σ_i in Å for each atom type in the all-atom protein model and van der Waals radii $\sigma_{vdw,i}$ (i.e., location of the minimum in the Lennard-Jones interatomic potential) from the Amber force field [48]. s indicates the ratio of the van der Waals radii to those used in the present study. The atom types with subscripts indicate an additional atom type when the main atom is bonded to the subscripted atom.

Atom type	Our all-atom protein model σ_i	Amber $\sigma_{vdw,i}$	s
C	1.5	1.7	1.1
C _O	1.3	1.7	1.3
O	1.4	1.5	1.1
N	1.3	1.6	1.2
H	1.1	1.0	0.9
H _N	1.0	1.0	1.0

TABLE IV. The 50 proteins that we simulated using the all-atom model identified by their PDBIDs. We also provide the number of amino acids N_{aa} for each protein.

PDBID	N_{aa}								
2f60	60	5b8d	99	1e29	135	5ljp	168	4lgj	256
1utg	70	4kdw	102	4wee	135	3bwz	171	4r78	287
1cc8	72	1ifr	113	5juh	137	4n6q	178	1lzl	317
5hub	79	2igp	114	4ga2	144	5ckl	181	5dp2	335
5wd9	86	2opc	115	2iih	146	4o6u	182	1m15	356
4he6	89	3zsu	118	5cvw	150	3rlk	183	6o08	360
4ltt	91	2ckk	120	3zuc	153	6dnm	187	5mpr	364
4xxl	92	4o0a	123	1hzt	153	3boe	209	2aeu	366
1v05	96	6bl5	129	3k7i	157	1sdi	213	4xd1	397
4qnd	97	1vsr	134	2z6o	166	3dha	254	1q6z	524

as well as the particular side chain dihedral angle combinations observed in the cores of individual protein x-ray crystal structures [60–64]. Table IV shows the 50 randomly selected proteins that were studied with the all-atom protein model.

TABLE V. The relative hydrophobicity λ_i for each of the 20 amino acids indicated by their three-letter codes.

Residue	λ_i	Residue	λ_i	Residue	λ_i	Residue	λ_i
ARG	0.0	GLN	0.29	GLY	0.52	TRP	0.85
ASP	0.09	PRO	0.39	TYR	0.64	VAL	0.89
GLU	0.16	HIS	0.4	ALA	0.67	PHE	0.96
LYS	0.16	SER	0.42	CYS	0.74	LEU	0.97
ASN	0.25	THR	0.48	MET	0.84	ILE	1.0

The proteins are all single chain, high resolution, and have low sequence similarity as our large database of structures was culled from the Protein Data Bank using PISCES [65,66]. Lastly, in Table V, we provide the relative amino acid hydrophobicities λ_i . These values were obtained in a previous study that collected numerous amino acid hydrophobicity scales, normalized them between 0 and 1, and found the average value for each amino acid type [68].

[1] K. A. Dill, Dominant forces in protein folding, *Biochemistry* **29**, 7133 (1990).

[2] C. Chothia, Structural invariants in protein folding, *Nature (London)* **254**, 304 (1975).

[3] F. M. Richards, The interpretation of protein structures: Total volume, group volume distributions and packing density, *J. Mol. Biol.* **82**, 1 (1974).

[4] F. M. Richards, Areas, volumes, packing, and protein structure, *Annu. Rev. Biophys. Bioeng.* **6**, 151 (1977).

[5] M. Gerstein and C. Chothia, Packing at the protein-water interface., *Proc. Natl. Acad. Sci. USA* **93**, 10167 (1996).

[6] J. Tsai, R. Taylor, C. Chothia, and M. Gerstein, The packing density in proteins: Standard radii and volumes, *J. Mol. Biol.* **290**, 253 (1999).

[7] P. J. Fleming and F. M. Richards, Protein packing: Dependence on protein size, secondary structure and amino acid composition, *J. Mol. Biol.* **299**, 487 (2000).

[8] J. Liang and K. A. Dill, Are proteins well-packed? *Biophys. J.* **81**, 751 (2001).

[9] J. D. Bryngelson and P. G. Wolynes, Spin glasses and the statistical mechanics of protein folding, *Proc. Natl. Acad. Sci. USA* **84**, 7524 (1987).

[10] H. Frauenfelder, S. G. Sligar, and P. G. Wolynes, The energy landscapes and motions of proteins, *Science* **254**, 1598 (1991).

[11] P. E. Leopold, M. Montal, and J. N. Onuchic, Protein folding funnels: A kinetic approach to the sequence-structure relationship, *Proc. Natl. Acad. Sci. USA* **89**, 8721 (1992).

[12] P. G. Wolynes, J. N. Onuchic, and D. Thirumalai, Navigating the folding routes, *Science* **267**, 1619 (1995).

[13] J. D. Bryngelson, J. N. Onuchic, N. D. Socci, and P. G. Wolynes, Funnels, pathways, and the energy landscape of protein folding: A synthesis, *Proteins: Struct. Funct. Bioinf.* **21**, 167 (1995).

[14] J. N. Onuchic, Z. Luthey-Schulten, and P. G. Wolynes, Theory of protein folding: The energy landscape perspective, *Annu. Rev. Phys. Chem.* **48**, 545 (1997).

[15] S. S. Plotkin and J. N. Onuchic, Understanding protein folding with energy landscape theory part I: Basic concepts, *Q. Rev. Biophys.* **35**, 111 (2002).

[16] G. Lois, J. Bławdziewicz, and C. S. O’Hern, Reliable protein folding on complex energy landscapes: The free energy reaction path, *Biophys. J.* **95**, 2692 (2008).

[17] P. P. Jose and I. Andricioaei, Similarities between protein folding and granular jamming, *Nat. Commun.* **3**, 1161 (2012).

[18] J. C. Gaines, W. W. Smith, L. Regan, and C. S. O’Hern, Random close packing in protein cores, *Phys. Rev. E* **93**, 032415 (2016).

[19] J. C. Gaines, S. Acebes, A. Virrueta, M. Butler, L. Regan, and C. S. O’Hern, Comparing side chain packing in soluble proteins, protein-protein interfaces and transmembrane proteins, *Proteins: Struct. Funct. Bioinf.* **86**, 581 (2018).

[20] J. D. Treado, Z. Mei, L. Regan, and C. S. O’Hern, Void distributions reveal structural link between jammed packings and protein cores, *Phys. Rev. E* **99**, 022416 (2019).

[21] Z. Mei, J. D. Treado, A. T. Grigas, Z. A. Levine, L. Regan, and C. S. O’Hern, Analyses of protein cores reveal fundamental differences between solution and crystal structures, *Proteins: Struct. Funct. Bioinf.* **88**, 1154 (2020).

[22] A. T. Grigas, Z. Liu, L. Regan, and C. S. O’Hern, Core packing of well-defined x-ray and NMR structures is the same, *Protein Sci.* **31**, e4373 (2022).

[23] H. W. Cho, G. Shi, T. R. Kirkpatrick, and D. Thirumalai, Random first order transition theory for glassy dynamics in a single condensed polymer, *Phys. Rev. Lett.* **126**, 137801 (2021).

[24] A. T. Grigas, A. Fisher, M. D. Shattuck, and C. S. O’Hern, Connecting polymer collapse and the onset of jamming, *Phys. Rev. E* **109**, 034406 (2024).

[25] M. Ozawa, L. Berthier, and D. Coslovich, Exploring the jamming transition over a wide range of critical densities, *SciPost Phys.* **3**, 027 (2017).

- [26] E. Bitzek, P. Koskinen, F. Gähler, M. Moseler, and P. Gumbsch, Structural relaxation made simple, *Phys. Rev. Lett.* **97**, 170201 (2006).
- [27] M. P. Allen and D. J. Tildesley, *Computer Simulation of Liquids*, 2nd ed. (Oxford University Press, Oxford, 2017).
- [28] C. S. O'Hern, L. E. Silbert, A. J. Liu, and S. R. Nagel, Jamming at zero temperature and zero applied stress: The epitome of disorder, *Phys. Rev. E* **68**, 011306 (2003).
- [29] M. van Hecke, Jamming of soft particles: Geometry, mechanics, scaling and isostaticity, *J. Phys.: Condens. Matter* **22**, 033101 (2010).
- [30] A. J. Liu and S. R. Nagel, The jamming transition and the marginally jammed solid, *Annu. Rev. Condens. Matter Phys.* **1**, 347 (2010).
- [31] C. P. Goodrich, S. Dagois-Bohy, B. P. Tighe, M. van Hecke, A. J. Liu, and S. R. Nagel, Jamming in finite systems: Stability, anisotropy, fluctuations, and scaling, *Phys. Rev. E* **90**, 022138 (2014).
- [32] N. C. Karayiannis and M. Laso, Dense and nearly jammed random packings of freely jointed chains of tangent hard spheres, *Phys. Rev. Lett.* **100**, 050602 (2008).
- [33] N. C. Karayiannis, K. Foteinopoulou, and M. Laso, The structure of random packings of freely jointed chains of tangent hard spheres, *J. Chem. Phys.* **130**, 164908 (2009).
- [34] R. S. Hoy, Jamming of semiflexible polymers, *Phys. Rev. Lett.* **118**, 068002 (2017).
- [35] S. M. Soik and T. A. Sharp, Effects of spherical confinement and backbone stiffness on flexible polymer jamming, *Phys. Rev. E* **99**, 052505 (2019).
- [36] L. E. Silbert, A. J. Liu, and S. R. Nagel, Vibrations and diverging length scales near the unjamming transition, *Phys. Rev. Lett.* **95**, 098301 (2005).
- [37] M. Wyart, L. E. Silbert, S. R. Nagel, and T. A. Witten, Effects of compression on the vibrational modes of marginally jammed solids, *Phys. Rev. E* **72**, 051306 (2005).
- [38] P. Charbonneau, E. I. Corwin, G. Parisi, A. Poncet, and F. Zamponi, Universal non-debye scaling in the density of states of amorphous solids, *Phys. Rev. Lett.* **117**, 045503 (2016).
- [39] S. Henkes, C. Brito, and O. Dauchot, Extracting vibrational modes from fluctuations: A pedagogical discussion, *Soft Matter* **8**, 6092 (2012).
- [40] T. Bertrand, C. F. Schreck, C. S. O'Hern, and M. D. Shattuck, Hypocoordinated solids in particulate media, *Phys. Rev. E* **89**, 062203 (2014).
- [41] Q. Wu, T. Bertrand, M. D. Shattuck, and C. S. O'Hern, Response of jammed packings to thermal fluctuations, *Phys. Rev. E* **96**, 062902 (2017).
- [42] B. Lee and F. Richards, The interpretation of protein structures: Estimation of static accessibility, *J. Mol. Biol.* **55**, 379 (1971).
- [43] S. Mitternacht, FreeSASA: An open source C library for solvent accessible surface area calculations, *F1000Research* **5**, 189 (2016).
- [44] C. Rycroft, Voro++: A three-dimensional Voronoi cell library in C++, <https://www.osti.gov/biblio/946741> (2009).
- [45] N. Xu, M. Wyart, A. J. Liu, and S. R. Nagel, Excess vibrational modes and the boson peak in model glasses, *Phys. Rev. Lett.* **98**, 175502 (2007).
- [46] A. Lappala, A. Zaccone, and E. M. Terentjev, Polymer glass transition occurs at the marginal rigidity point with connectivity $z^* = 4$, *Soft Matter* **12**, 7330 (2016).
- [47] J. D. Dietz and R. S. Hoy, Two-stage athermal solidification of semiflexible polymers and fibers, *Soft Matter* **16**, 6206 (2020).
- [48] A. v. Bondi, van der Waals volumes and radii, *J. Phys. Chem.* **68**, 441 (1964).
- [49] F. Jiang, W. Han, and Y.-D. Wu, The intrinsic conformational features of amino acids from a protein coil library and their applications in force field development, *Phys. Chem. Chem. Phys.* **15**, 3413 (2013).
- [50] I. W. Davis, A. Leaver-Fay, V. B. Chen, J. N. Block, G. J. Kapral, X. Wang, L. W. Murray, I. Arendall, W. Bryan, J. Snoeyink, J. S. Richardson, and D. C. Richardson, MolProbity: All-Atom contacts and structure validation for proteins and nucleic acids, *Nucl. Acids Res.* **35**, W375 (2007).
- [51] V. B. Chen, W. B. Arendall, III, J. J. Headd, D. A. Keedy, R. M. Immormino, G. J. Kapral, L. W. Murray, J. S. Richardson, and D. C. Richardson, MolProbity: All-Atom structure validation for macromolecular crystallography, *Acta Cryst. D* **66**, 12 (2010).
- [52] C. J. Williams, J. J. Headd, N. W. Moriarty, M. G. Prisant, L. L. Videau, L. N. Deis, V. Verma, D. A. Keedy, B. J. Hintze, V. B. Chen, S. Jain, S. M. Lewis, W. B. Arendall III, J. Snoeyink, P. D. Adams, S. C. Lovell, J. S. Richardson, and D. C. Richardson, Molprobity: More and better reference data for improved all-atom structure validation, *Protein Sci.* **27**, 293 (2018).
- [53] V. Hornak, R. Abel, A. Okur, B. Strockbine, A. Roitberg, and C. Simmerling, Comparison of multiple amber force fields and development of improved protein backbone parameters, *Proteins: Struct. Funct. Bioinf.* **65**, 712 (2006).
- [54] K. Lindorff-Larsen, S. Piana, K. Palmo, P. Maragakis, J. L. Klepeis, R. O. Dror, and D. E. Shaw, Improved side-chain torsion potentials for the Amber ff99SB protein force field, *Proteins: Struct. Funct. Bioinf.* **78**, 1950 (2010).
- [55] J. A. Maier, C. Martinez, K. Kasavajhala, L. Wickstrom, K. E. Hauser, and C. Simmerling, ff14sb: Improving the accuracy of protein side chain and backbone parameters from ff99sb, *J. Chem. Theor. Comput.* **11**, 3696 (2015).
- [56] C. Tian, K. Kasavajhala, K. A. A. Belfon, L. Raguette, H. Huang, A. N. Migués, J. Bickel, Y. Wang, J. Pincay, Q. Wu, and C. Simmerling, ff19SB: Amino-acid-specific protein backbone parameters trained against quantum mechanics energy surfaces in solution, *J. Chem. Theor. Comput.* **16**, 528 (2020).
- [57] A. D. Mackerell Jr., M. Feig, and C. L. Brooks III, Extending the treatment of backbone energetics in protein force fields: Limitations of gas-phase quantum mechanics in reproducing protein conformational distributions in molecular dynamics simulations, *J. Comput. Chem.* **25**, 1400 (2004).
- [58] G. Ramachandran, C. Ramakrishnan, and V. Sasisekharan, Stereochemistry of polypeptide chain configurations, *J. Mol. Biol.* **7**, 95 (1963).
- [59] C. Ramakrishnan and G. Ramachandran, Stereochemical criteria for polypeptide and protein chain conformations. II. Allowed conformations for a pair of peptide units, *Biophys. J.* **5**, 909 (1965).

- [60] A. Q. Zhou, C. S. O'Hern, and L. Regan, The power of hard-sphere models: Explaining side-chain dihedral angle distributions of Thr and Val, *Biophys. J.* **102**, 2345 (2012).
- [61] A. Q. Zhou, C. S. O'Hern, and L. Regan, Predicting the side-chain dihedral angle distributions of nonpolar, aromatic, and polar amino acids using hard sphere models, *Proteins: Struct. Funct. Bioinf.* **82**, 2574 (2014).
- [62] D. Caballero, J. Määttä, A. Q. Zhou, M. Sammalkorpi, C. S. O'Hern, and L. Regan, Intrinsic α -helical and β -sheet conformational preferences: A computational case study of alanine, *Protein Sci.* **23**, 970 (2014).
- [63] D. Caballero, A. Virrueta, C. O'Hern, and L. Regan, Steric interactions determine side-chain conformations in protein cores, *Protein Eng. Des. Sel.* **29**, 367 (2016).
- [64] J. C. Gaines, A. Virrueta, D. A. Buch, S. J. Fleishman, C. S. O'Hern, and L. Regan, Collective repacking reveals that the structures of protein cores are uniquely specified by steric repulsive interactions, *Protein Eng. Des. Sel.* **30**, 387 (2017).
- [65] G. Wang and R. L. Dunbrack, Jr., PISCES: A protein sequence culling server, *Bioinformatics* **19**, 1589 (2003).
- [66] G. Wang and R. L. Dunbrack Jr., PISCES: Recent improvements to a PDB sequence culling server, *Nucl. Acids Res.* **33**, W94 (2005).
- [67] J. Word, S. C. Lovell, J. S. Richardson, and D. C. Richardson, Asparagine and glutamine: Using hydrogen atom contacts in the choice of side-chain amide orientation, *J. Mol. Biol.* **285**, 1735 (1999).
- [68] W. W. Smith, P.-Y. Ho, and C. S. O'Hern, Calibrated Langevin-dynamics simulations of intrinsically disordered proteins, *Phys. Rev. E* **90**, 042709 (2014).
- [69] T. Lubensky, C. Kane, X. Mao, A. Souslov, and K. Sun, Phonons and elasticity in critically coordinated lattices, *Rep. Prog. Phys.* **78**, 073901 (2015).
- [70] M. Mailman, C. F. Schreck, C. S. O'Hern, and B. Chakraborty, Jamming in systems composed of frictionless ellipse-shaped particles, *Phys. Rev. Lett.* **102**, 255501 (2009).
- [71] C. F. Schreck, M. Mailman, B. Chakraborty, and C. S. O'Hern, Constraints and vibrations in static packings of ellipsoidal particles, *Phys. Rev. E* **85**, 061305 (2012).
- [72] K. Lindorff-Larsen, S. Piana, R. O. Dror, and D. E. Shaw, How fast-folding proteins fold, *Science* **334**, 517 (2011).
- [73] R. B. Best and G. Hummer, Optimized molecular dynamics force fields applied to the helix coil transition of polypeptides, *J. Phys. Chem. B* **113**, 9004 (2009).
- [74] W. L. Jorgensen, Quantum and statistical mechanical studies of liquids. 10. Transferable intermolecular potential functions for water, alcohols, and ethers. Application to liquid water, *J. Am. Chem. Soc.* **103**, 335 (1981).
- [75] P. Mark and L. Nilsson, Structure and Dynamics of the TIP3P, SPC, and SPC/E Water Models at 298 K, *J. Phys. Chem. A* **105**, 9954 (2001).
- [76] G. Bussi, D. Donadio, and M. Parrinello, Canonical sampling through velocity rescaling, *J. Chem. Phys.* **126**, 014101 (2007).
- [77] A. N. Naganathan and V. Muñoz, Scaling of folding times with protein size, *J. Am. Chem. Soc.* **127**, 480 (2005).
- [78] A. Santos, S. B. Yuste, M. López de Haro, G. Odriozola, and V. Ogarko, Simple effective rule to estimate the jamming packing fraction of polydisperse hard spheres, *Phys. Rev. E* **89**, 040302(R) (2014).
- [79] A. Donev, R. Connelly, F. H. Stillinger, and S. Torquato, Underconstrained jammed packings of nonspherical hard particles: Ellipses and ellipsoids, *Phys. Rev. E* **75**, 051304 (2007).
- [80] Y. Yuan, K. Van der Werf, M. D. Shattuck, and C. S. O'Hern, Jammed packings of 3d superellipsoids with tunable packing fraction, coordination number, and ordering, *Soft Matter* **15**, 9751 (2019).
- [81] Y. Jiao and S. Torquato, Maximally random jammed packings of platonic solids: Hyperuniform long-range correlations and isostaticity, *Phys. Rev. E* **84**, 041309 (2011).
- [82] C. Song, P. Wang, and H. A. Makse, A phase diagram for jammed matter, *Nature (London)* **453**, 629 (2008).
- [83] L. E. Silbert, Jamming of frictional spheres and random loose packing, *Soft Matter* **6**, 2918 (2010).
- [84] J. C. Gaines, A. H. Clark, L. Regan, and C. S. O'Hern, Packing in protein cores, *J. Phys.: Condens. Matter* **29**, 293001 (2017).
- [85] D. Wang, J. D. Treado, A. Boromand, B. Norwick, M. P. Murrell, M. D. Shattuck, and C. S. O'Hern, The structural, vibrational, and mechanical properties of jammed packings of deformable particles in three dimensions, *Soft Matter* **17**, 9901 (2021).
- [86] A. D. Griffith and R. S. Hoy, Densest versus jammed packings of bent-core trimers, *Phys. Rev. E* **100**, 022903 (2019).
- [87] G.-J. Gao, J. Bławdziewicz, and C. S. O'Hern, Frequency distribution of mechanically stable disk packings, *Phys. Rev. E* **74**, 061304 (2006).
- [88] P. Chaudhuri, L. Berthier, and S. Sastry, Jamming transitions in amorphous packings of frictionless spheres occur over a continuous range of volume fractions, *Phys. Rev. Lett.* **104**, 165701 (2010).
- [89] S. S. Ashwin, M. Zaeifi Yamchi, and R. K. Bowles, Inherent structure landscape connection between liquids, granular materials, and the jamming phase diagram, *Phys. Rev. Lett.* **110**, 145701 (2013).
- [90] T. Bertrand, R. P. Behringer, B. Chakraborty, C. S. O'Hern, and M. D. Shattuck, Protocol dependence of the jamming transition, *Phys. Rev. E* **93**, 012901 (2016).
- [91] H. Yamada, T. Nagae, and N. Watanabe, High-pressure protein crystallography of hen egg-white lysozyme, *Acta Cryst. D* **71**, 742 (2015).
- [92] M. R. Mitchell, T. Tlusty, and S. Leibler, Strain analysis of protein structures and low dimensionality of mechanical allosteric couplings, *Proc. Natl. Acad. Sci. USA* **113**, E5847 (2016).
- [93] R. L. Baldwin, C. Frieden, and G. D. Rose, Dry molten globule intermediates and the mechanism of protein unfolding, *Proteins: Struct. Funct. Bioinf.* **78**, 2725 (2010).
- [94] S. K. Jha and J. B. Udgaonkar, Direct evidence for a dry molten globule intermediate during the unfolding of a small protein, *Proc. Natl. Acad. Sci. USA* **106**, 12289 (2009).
- [95] S. S. Sarkar, J. B. Udgaonkar, and G. Krishnamoorthy, Unfolding of a small protein proceeds via dry and wet globules and a solvated transition state, *Biophys. J.* **105**, 2392 (2013).
- [96] S. Neumaier and T. Kiefhaber, Redefining the dry molten globule state of proteins, *J. Mol. Biol.* **426**, 2520 (2014).
- [97] C. B. Wilson, W.-M. Yau, and R. Tycko, Experimental evidence for millisecond–timescale structural evolution following the microsecond–timescale folding of a small protein, *Phys. Rev. Lett.* **132**, 048402 (2024).

- [98] X. Hu, L. Hong, M. Dean Smith, T. Neusius, X. Cheng, and J. C. Smith, The dynamics of single protein molecules is non-equilibrium and self-similar over thirteen decades in time, *Nat. Phys.* **12**, 171 (2016).
- [99] J. Li, J. Xie, A. Godec, K. R. Weninger, C. Liu, J. C. Smith, and L. Hong, Non-ergodicity of a globular protein extending beyond its functional timescale, *Chem. Sci.* **13**, 9668 (2022).
- [100] Q. Liao, L. Berthier, H.-J. Zhou, and N. Xu, Dynamic Gardner cross-over in a simple glass, *Proc. Natl. Acad. Sci. USA* **120**, e2218218120 (2023).
- [101] E. Dorbath, A. Gulzar, and G. Stock, Log-periodic oscillations as real-time signatures of hierarchical dynamics in proteins, *J. Chem. Phys.* **160**, 074103 (2024).
- [102] C. P. Goodrich, A. J. Liu, and S. R. Nagel, Solids between the mechanical extremes of order and disorder, *Nat. Phys.* **10**, 578 (2014).
- [103] J. Xu, W. A. Baase, E. Baldwin, and B. W. Matthews, The response of T4 lysozyme to large-to-small substitutions within the core and its relation to the hydrophobic effect, *Protein Sci.* **7**, 158 (1998).
- [104] R. Liu, W. A. Baase, and B. W. Matthews, The introduction of strain and its effects on the structure and stability of T4 lysozyme, *J. Mol. Biol.* **295**, 127 (2000).
- [105] W. A. Baase, L. Liu, D. E. Tronrud, and B. W. Matthews, Lessons from the lysozyme of phage T4, *Protein Sci.* **19**, 631 (2010).
- [106] J. Chen, N. Sawyer, and L. Regan, Protein–protein interactions: General trends in the relationship between binding affinity and interfacial buried surface area, *Protein Sci.* **22**, 510 (2013).
- [107] C. M. Davis, M. Gruebele, and S. Sukenik, How does solvation in the cell affect protein folding and binding? *Curr. Opin. Struct. Biol.* **48**, 23 (2018).
- [108] S. Perticaroli, J. D. Nickels, G. Ehlers, H. O'Neill, Q. Zhang, and A. P. Sokolov, Secondary structure and rigidity in model proteins, *Soft Matter* **9**, 9548 (2013).
- [109] S. Perticaroli, J. D. Nickels, G. Ehlers, and A. P. Sokolov, Rigidity, secondary structure, and the universality of the boson peak in proteins, *Biophys. J.* **106**, 2667 (2014).
- [110] A. Markelz, S. Whitmire, J. Hillebrecht, and R. Birge, Thz time domain spectroscopy of biomolecular conformational modes, *Phys. Med. Biol.* **47**, 3797 (2002).
- [111] A. Leitenstorfer, A. S. Moskalenko, T. Kampfrath, J. Kono, E. Castro-Camus, K. Peng, N. Qureshi, D. Turchinovich, K. Tanaka, A. G. Markelz, M. Havenith, C. Hough, H. J. Joyce, W. J. Padilla, B. Zhou, K.-Y. Kim, X.-C. Zhang, P. U. Jepsen, S. Dhillon, M. Vitiello *et al.*, The 2023 terahertz science and technology roadmap, *J. Phys. D* **56**, 223001 (2023).
- [112] <https://github.com/agrigas115/HS-HP>